Electron Tomographic Analysis of Somatic Cell Plate Formation in Meristematic Cells of Arabidopsis Preserved by High-Pressure Freezing [W]

José M. Seguí-Simarro, Jotham R. Austin II, Erin A. White, and L. Andrew Staehelin[1]

Department of Molecular, Cellular, and Developmental Biology, University of Colorado, Boulder, Colorado 80309-0347

We have investigated the process of somatic-type cytokinesis in Arabidopsis (*Arabidopsis thaliana*) meristem cells with a three-dimensional resolution of ~7 nm by electron tomography of high-pressure frozen/freeze-substituted samples. Our data demonstrate that this process can be divided into four phases: phragmoplast initials, solid phragmoplast, transitional phragmoplast, and ring-shaped phragmoplast. Phragmoplast initials arise from clusters of polar microtubules (MTs) during late anaphase. At their equatorial planes, cell plate assembly sites are formed, consisting of a filamentous ribosome-excluding cell plate assembly matrix (CPAM) and Golgi-derived vesicles. The CPAM, which is found only around growing cell plate regions, is suggested to be responsible for regulating cell plate growth. Virtually all phragmoplast MTs terminate inside the CPAM. This association directs vesicles to the CPAM and thereby to the growing cell plate. Cell plate formation within the CPAM appears to be initiated by the tethering of vesicles by exocyst-like complexes. After vesicle fusion, hourglass-shaped vesicle intermediates are stretched to dumbbells by a mechanism that appears to involve the expansion of dynamin-like springs. This stretching process reduces vesicle volume by ~50%. At the same time, the lateral expansion of the phragmoplast initials and their CPAMs gives rise to the solid phragmoplast. Later arriving vesicles begin to fuse to the bulbous ends of the dumbbells, giving rise to the tubulo-vesicular membrane network (TVN). During the transitional phragmoplast stage, the CPAM and MTs disassemble and then reform in a peripheral ring phragmoplast configuration. This creates the centrifugally expanding peripheral cell plate growth zone, which leads to cell plate fusion with the cell wall. Simultaneously, the central TVN begins to mature into a tubular network, and ultimately into a planar fenestrated sheet (PFS), through the removal of membrane via clathrin-coated vesicles and by callose synthesis. Small secondary CPAMs with attached MTs arise de novo over remaining large fenestrae to focus local growth to these regions. When all of the fenestrae are closed, the new cell wall is complete. Few endoplasmic reticulum (ER) membranes are seen associated with the phragmoplast initials and with the TVN cell plate that is formed within the solid phragmoplast. ER progressively accumulates thereafter, reaching a maximum during the late PFS stage, when most cell plate growth is completed.

INTRODUCTION

In plants, cytokinesis partitions the cytoplasm of a dividing cell by forming a new cell wall between the two daughter nuclei. In somatic cells, the new cell wall is produced by means of a cell plate, which forms in the equatorial plane of a cytoskeletal array known as a phragmoplast. This process has been a major focus of research of plant biologists for more than a century. Indeed, the term cell plate can be traced to Strasburger (1875), who also reported that the cell plate arose within a system of fibrils, named a phragmoplast by Errera (1888). Similarly, the notion that cell plates were formed by the fusion of petite vacuoles (vesicles) predates the modern era of plant cytokinesis research (Becker, 1932).

The first electron microscope (EM) analyses of chemically preserved cells in the 1950s both verified these previous concepts and demonstrated that the coalescing vesicles gave rise to the cell plate membrane, ultimately becoming the plasma membranes, whereas the vesicle contents are converted into cell walls (Buvat and Puissant, 1958; Porter and Caulfield, 1958; Porter and Machado, 1960). In 1963, the Golgi stacks (dictyosomes) were identified as the source of the cell plate–forming vesicles (Whaley and Mollenhauer, 1963), and the microtubular nature of the phragmoplast was established (Ledbetter and Porter, 1963). In 1967 and 1968, Hepler and coworkers published their now classic papers on somatic and syncytial-type cell plate formation, demonstrating that cell plate assembly involved structural intermediates that were inconsistent with the simple vesicle coalescence model. This was followed by a series of studies shedding light on the early formation of the first microtubular and membranous arrays at the plane of cell division (Bajer, 1968; Hepler and Jackson, 1968; Brown and Lemmon, 1991) and the association of the cell plate with other membranous systems, such as the endoplasmic reticulum (ER) (Hepler, 1982). In the following years, numerous studies of the process of cell division in living cells by means of a variety of light

microscope techniques (Baskin and Cande, 1990; Zhang et al., 1990; Asada et al., 1991; Schopfer and Hepler, 1991; Assaad, 2001; Molchan et al., 2002) led to the following consensus model of plant cytokinesis: cytokinesis starts in late anaphase with the formation of the phragmoplast from anaphase spindle microtubules. The phragmoplast consists of two opposing arrays of actin filaments and microtubules with their (+) ends facing the plane of division. Its primary function is to transport Golgi-derived vesicles to the site of cell plate assembly. Formation of the cell plate involves vesicle fusion, starting in the center of the phragmoplast and expanding by centrifugal growth. During later stages of this growth, the MTs depolymerize in the central region and new ones form around the cell plate margins, directing the vesicles to these growing regions. This continues until the cell plate fuses with the parent cell wall. More recent studies also have examined the role of specific molecules in cell plate formation (reviewed in Verma, 2001; Bednarek and Falbel, 2002). In parallel, the characterization of cytokinesis mutants has contributed significantly to a better understanding of this important cellular process (Lauber et al., 1997; Nacry et al., 2000; Waizenegger et al., 2000; Sollner et al., 2002).

The introduction of high-pressure freezing/freeze substitution methods for preserving cells for ultrastructural analysis (Gilkey and Staehelin, 1986) ushered in a new era of EM studies of plant cytokinesis because these techniques can capture and stabilize transient cell plate and phragmoplast structures. With these techniques, it became possible not only to characterize more precisely the major cytoskeletal structures and membrane network intermediates associated with cell plate assembly but also to deduce how callose provides the spreading force to convert tubular membrane networks into planar fenestrated sheets (Samuels et al., 1995; Rensing et al., 2002). With the principal specimen preparation problem solved, electron microscopists were able to focus their efforts on the last major hurdle for understanding the three-dimensional (3-D) architecture of cell plates, the section thickness–based limitation of the z axis resolution of the micrographs. This z axis resolution limitation can now be overcome by means of dual-axis electron tomography, which yields tomographic slices as thin as 2 nm and a 3-D resolution of ∼7 nm (Kremer et al., 1996; Ladinsky et al., 1999). The combination of all of these techniques has been exploited recently to obtain new insights into the formation of syncytial-type cell plates in the Arabidopsis (*Arabidopsis thaliana*) endosperm and pollen cells (Otegui et al., 2001; Otegui and Staehelin, 2004).

In this study, we have employed these advanced structural research tools to investigate the 3-D architecture of structures involved in cell plate and cell wall assembly in shoot and root apical meristem cells of Arabidopsis. Our data not only provide more detailed quantitative and 3-D information on the different cell plate membrane networks described by Samuels et al. (1995) but also have yielded numerous novel insights into the processes that govern cell plate assembly and maturation. For example, our tomograms have enabled us to visualize putative plant exocyst-like complexes that tether the cell plate–forming vesicles before fusion as well as intermediates in the process of dumbbell vesicle formation, which exhibit both compressed and expanded dynamin-like springs. In addition, they have provided evidence

that the cell plate assembly matrix (CPAM; Otegui and Staehelin, 2004) plays a role in regulating both cell plate assembly and the organization of the phragmoplast microtubules. Finally, we have been able to document in considerable detail the changing spatial relationships between ER cisternae and the different cell plate membrane networks. For technical reasons, the phragmoplast-associated actin filaments, which also play a critical role in cell plate formation (Molchan et al., 2002), have not been reconstructed and are therefore not shown in our models.

RESULTS

This study reports on the 3-D architecture of somatic-type cell plates in apical meristem cells of Arabidopsis analyzed by means of dual-axis electron tomography of high-pressure frozen/freeze-substituted shoot and root samples. No differences were detected in cell plate formation between shoot and root meristematic cells. Therefore, we used both samples interchangeably for this study. The results are based on the tomographic analysis of 15 cells and an additional set of ∼400 EM micrographs of >200 different cell plates covering all of the stages of cell plate formation. As documented by Samuels et al. (1995), somatic-type cell plate formation progresses via a precise set of assembly intermediates. Our new observations have enabled us not only to understand how these cell plate assembly intermediates fit into the larger scheme of cytokinesis but also to gain a deeper understanding of the mechanisms that drive the assembly process.

Cell Plates Are Formed by Two Types of Vesicles: Small-Dark and Large-Light

Cytokinesis starts during anaphase with the accumulation of vesicles at the site of the future cell wall and the beginning of vesicle fusion and dumbbell formation (Figure 1). As the separating chromosomes approach the spindle poles, the individual clusters of remaining polar microtubules (MTs) become integrated into the phragmoplast initials, which mediate the transport of the first Golgi-derived vesicles to the site of cell plate assembly. At that site, cell plate assembly starts with the fusion of the first vesicles and the transformation of the fused vesicles into dumbbells, the building blocks of the initial cell plate–forming membrane networks. All of these early cell plate growth events take place within a distinct, ribosome-excluding (Figure 7D) cytoplasmic matrix, the CPAM (Otegui and Staehelin, 2004), which is described in greater detail below. Within and around the CPAMs, the resulting anaphase vesicle clouds contain two types of vesicles that can be distinguished by their size and by the staining of their contents. The smaller (∼51 nm in diameter) dark vesicles (Figures 2A to 2C) correspond to the green vesicles of Figures 1C and 1D, whereas the larger (∼66 nm in diameter) and lighter vesicles (Figures 2A, 2D, and 2E) correspond to the blue vesicles of Figures 1C and 1E.

Both types of cell plate–forming vesicles are found intermixed during all stages of somatic-type cell plate assembly (Figures 3 to 8). However, the ratio of the two types of vesicles varies among the different assembly stages (Figure 3). During the anaphase vesicle cloud and the following tubulo-vesicular network (TVN)
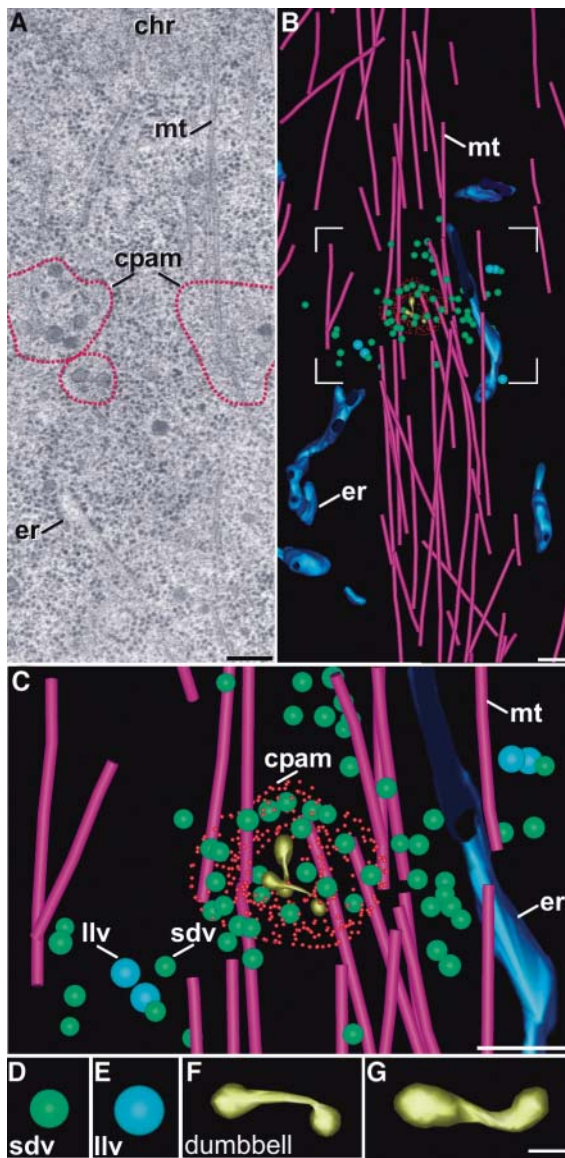
Figure 1. Phragmoplast Initials.

(A) Shoot apical meristem cell. EM micrograph showing a vesicle cloud surrounded by the CPAM. Spindle MTs extend from the segregating chromosomes (chr) to the CPAM.

(B) to **(G)** Root meristematic cell.

(B) Model view of a root meristematic cell phragmoplast initial with its associated vesicles and CPAM.

(C) Detail of the region boxed in **(B)**. Cell plate–forming vesicles (green small-dark (sdv) and large-light (llv); see also Figure 2) are seen both outside and inside the CPAM, whereas the dumbbell vesicles are confined to the CPAM. ER is excluded from the CPAM region.

(D) to **(G)** Enlargements of small-dark (sdv) **(D)**, large-light (llv) **(E)**, and dumbbell (**[F]** and **[G]**) vesicles.

Bars in **(A)** to **(C)** = 200 nm; bar in **(G)** = 50 nm for **(D)** to **(G)**.

stage (early telophase), the number of large-light vesicles is small (~7%) compared with the number of small-dark vesicles (~93%). However, when the cell plate reaches the tubular network (TN) stage and thereafter, the percentage of large-light vesicles increases to ~60%, and the number of small-dark vesicles decreases to ~40%.

To determine the origin of the two types of vesicles, we compared the vesicles in the vicinity of the Golgi stacks near the spindle poles with those closer to the cell plates. Even though all of the vesicles close to the Golgi stacks were of the small-dark type, both types of vesicles were always seen around the cell plates (data not shown). This suggested that the large-light vesicles were formed during vesicle trafficking between the Golgi stacks and the cell plate assembly sites. Further insights into the origin of the large-light vesicles came from calculations of their surface area and their volume. Thus, a large-light vesicle has on average ~2 times the surface area of a small-dark vesicle (~13,400 nm^2 versus ~7100 nm^2), and its volume is ~2.6 times larger than the volume of a small-dark vesicle (~147,000 nm^3 versus ~56,000 nm^3). Geometrical calculations predict that a large sphere with twice the surface area of a small sphere should have a 2.8 times larger volume than the small sphere (surface area increases by $radius^2$, and volume increases by $radius^3$). Based on these data and the discovery of hourglass-shaped putative vesicle fusion intermediates (surface area ~14,500 nm^2) with lighter stained contents (Figure 6A), we postulate that the large-light vesicles arise from the fusion of two small-dark vesicles as they traffic to the cell plate. The reduced staining would be consistent with the dilution of the vesicle
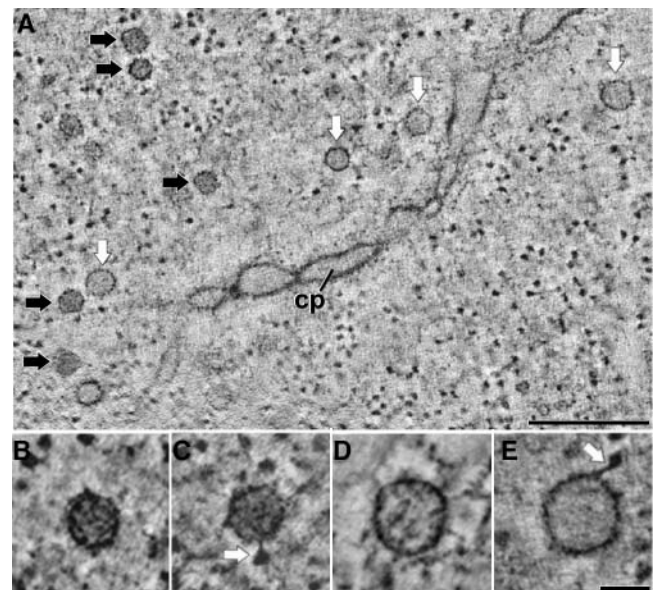
Figure 2. Two Different Types of Vesicles in the Vicinity of the Cell Plate.

The black arrows in **(A)** point to small-dark vesicles, and the white arrows point to large-light vesicles. Examples of small, dense vesicles (**[B]** and **[C]**) and large-light vesicles (**[D]** and **[E]**). Arrows in **(C)** and **(E)** point to L-shaped complexes (see also Figures 4A to 4H). cp, cell plate. Bar in **(A)** = 200 nm; bar in **(E)** = 50 nm for **(B)** to **(E)**.
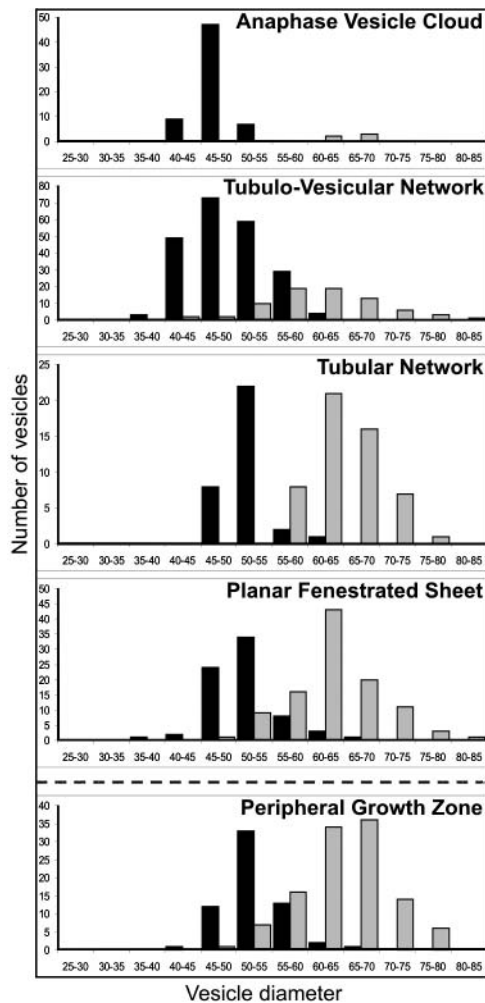
Figure 3. Vesicle Diameter Distribution during Cytokinetic Stages.

Histograms of the size distribution of cell plate–forming vesicles during different stages of cell plate formation. The individual bars indicate the number of vesicles per 5-nm diameter interval. Closed bars, small-dark vesicles; shaded bars, large-light vesicles.

contents as the volume increases. Of the 1019 vesicles identified in the tomograms produced for this study, only three exhibited an hourglass morphology as depicted in Figure 6A. This low number suggests that the formation of the large-light vesicles is a fast process. It also explains why such hourglass structures have not previously been observed in dividing somatic cells.

Many Cell Plate–Forming Vesicles within the CPAM Are Connected by Y-Shaped Molecular Complexes

Formation of a cell plate from Golgi-derived vesicles requires homotypic vesicle fusion and the concomitant formation of a membrane network in the plane of the future cell wall. Our data suggest that vesicles become linked by molecular complexes within the CPAM before fusion and that precursor forms of this putative tethering complex become attached to the vesicles

before they enter the CPAM. The structural characterization of the tethering complex is presented in Figures 4A to 4V, and the spatial distribution of the tethered vesicles in the context of a modeled cell plate is shown in Figure 4W.

Figures 4A to 4D illustrate a set (every fifth slice) of 2-nm-thick tomographic slices through a small-dark vesicle with a characteristic L-shaped molecular complex (Figure 4E) extending from its surface. These L-shaped complexes are most readily identified in views in which a dense round knob is seen to be connected through a thin rod-like filament to the vesicle surface (Figures 2C, 2E, 4A, and 4B). When these structures were tracked through tomographic slices (Figures 4A to 4D, beige arrows), the knob-like domain extended across ∼15 slices (30 nm), and the rod-like linker through two to three slices (∼4 to 6 nm). Using the slicer tool included in the 3dmod program of the IMOD package (Mastronarde, 1997; Otegui et al., 2001), one can rotate the vesicle around the axis of the rod-like linker domain to produce a side view that shows an L-shaped complex (Figure 4E). Three corresponding views of the modeled L-shaped complex are shown in Figures 4F to 4H. The axial length of the molecule is ∼35 nm. L-shaped complexes were present on ∼30% of the vesicles analyzed, attached mostly to small-dark vesicles (Figures 2C, 4A to 4E, and 4W). However, some were also found bound to large-light vesicles (Figures 2E and 4W).

Figures 4I to 4M illustrate two vesicles with two types of surface-associated filamentous structures (see also Supplemental Video Sequence 1 online). The structure highlighted by the beige arrows corresponds to an L-shaped complex (cf. Figures 4A to 4H with Figures 4I to 4P), whereas the structure marked by the purple arrows corresponds to a tethering complex between the two vesicles (Figures 4I to 4P) with an axial length of ∼35 nm. Modeled images of these structures are depicted in Figures 4N to 4P. Once properly oriented, these complexes exhibit distinct Y-shaped architecture with the two arms attached to the vesicles, as shown in Figure 4M. Careful analysis of all of the vesicle pairs connected in this manner showed that they always exhibited the same spatial relationship to the arms of the Y-shaped complexes and were separated by the same distance (∼20 nm), consistent with the hypothesis that they represent vesicle tethering complexes. Additional side view images of such linker complexes are illustrated in Figures 4Q to 4S. Together, these images strongly resemble the images of purified sec6/8 complexes (Figures 4T to 4V; Hsu et al., 1998), the mammalian counterpart of the yeast (*Saccharomyces cerevisiae*) membrane-tethering exocyst complex, in both morphology and length (∼35 nm versus ∼30 nm of the sec6/8 complex). Our tomograms also contain examples of three vesicles simultaneously connected through two separate sets of putative tethering complexes (data not shown).

Formation and Growth of Cell Plate–Forming Membrane Networks Occur within a CPAM

The fusion of vesicles, their transformation into dumbbells, and the joining of more vesicles to the dumbbells (see next section) take place within a distinct, ribosome-excluding (Figure 7D) cytoplasmic matrix, the CPAM. This cocoon-like matrix delineates not only where the vesicles fuse but also the general planar
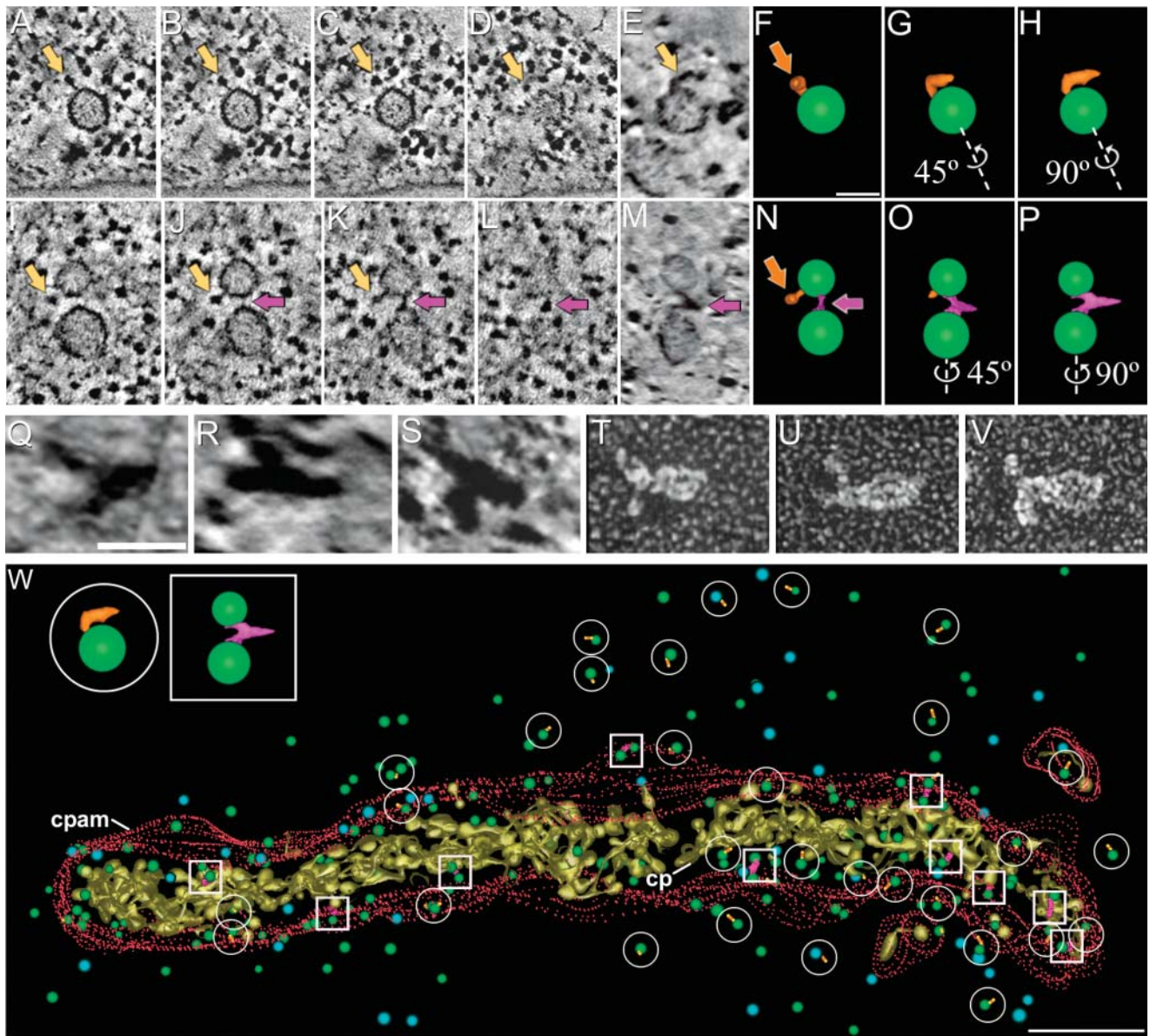
Figure 4. Tomographic Analysis of Putative Vesicle Tethering Complexes and Their Distribution in Relation to a CPAM and a Cell Plate.

(A) to **(D)** Vesicle-associated L-shaped complex (beige arrows) as seen in a series of tomographic slices taken every five slices.

(E) to **(H)** Slicer-tilted image showing a face-on view of the complex, which is depicted in modeled form in **(F)** to **(H)** with no tilt **(F)**, 45° tilt **(G)**, and 90° tilt **(H)**.

(I) to **(L)** Tomographic slice images of two vesicles connected by a Y-shaped tethering complex (purple arrows). The upper vesicle also carries an L-shaped complex (yellow arrow).

(M) to **(P)** Slicer-tilted image showing a face-on view of the Y-shaped tether, which is depicted in modeled form in **(N)** to **(P)** with no tilt **(N)**, 45° tilt **(O)**, and 90° tilt **(P)**.

(Q) to **(S)** Face-on views of Y-shaped tethering complexes as seen in tomographic slices.

(T) to **(V)** Images of glutaraldehyde-fixed purified Sec6/8 tethering complexes from mammalian brain (courtesy of J. Heuser, with permission).

(W) Distribution of L- and Y-shaped complexes around a CPAM containing a TVN stage cell plate (cp). Note that whereas the vesicles with L-shaped complexes (circles) are seen both outside and inside the CPAM, Y-shaped tethers (squares) are found only within the CPAM.

Bar in **(F)** = 50 nm for **(A)** to **(P)**; bar in **(Q)** = 25 nm for **(Q)** to **(V)**; bar in **(W)** = 500 nm.

organization of the membrane networks that give rise to the cell plate (Figures 1C, 4W, 6P, 7C, and 7E). The CPAM is not a solid structure but a fine filamentous (Figures 7C and 9A) ribosome exclusion zone. For this reason, we defined the boundaries of the CPAM as the interface between the ribosome-free zone and the ribosome-rich cytosol. This interface is modeled in the form of small red dots, as in previous studies (Otegui et al., 2001; Otegui and Staehelin, 2004).

The importance of the CPAM for defining where vesicles fuse is documented in Figure 4W. This model maps the spatial distribution of vesicles carrying L-shaped appendages and vesicle pairs connected by Y-shaped linkers with respect to the CPAM surrounding a TVN-type cell plate (Figures 4W and 7A). In Figure 4W, the vesicles with L-shaped extensions have been highlighted by circles, and the vesicles connected by Y-shaped linkers by squares. Note that the vesicles with L-shaped extensions are seen both outside and inside the CPAM, whereas all of the linked vesicles seem to be located exclusively within the CPAM.

The very first cell plate–forming dumbbells (Figures 1C, 1F, and 1G) are detected during late anaphase within small CPAMs located in the midzone of the phragmoplast initials (Figure 1C). These CPAMs form concomitantly with the arrival of the first cell plate–forming vesicles at the cell plate assembly site (Otegui and Staehelin, 2004). Furthermore, such CPAMs encompass all of the sites where new vesicles seem to fuse with the cell plate (Figures 1, 4W, 7D, 9C, and 9D). Figure 7E highlights the fact that even dumbbells that arise at a distance from the cell plate edge are always encompassed by a distinct CPAM. During the ring phragmoplast stage of cytokinesis, CPAM domains are seen not only over the least mature peripheral cell plate regions but also in island-like configurations over large fenestrae that require additional membrane material to close the remaining cell plate holes (Figures 9C and 9D). Most of the phragmoplast MT (+) ends terminate in the peripheral regions of CPAMs (Figures 6P, 7C, and 9A). This structural association of the MTs with the CPAM may ensure that vesicles traveling along MTs are delivered to the CPAM regions where cell plate growth occurs.

Quantitative analysis of the average width of the CPAMs associated with different stages of cell plate formation (Figure 5) shows that their average width increases from ~115 nm during the anaphase vesicle cloud stage to ~155 nm during the TVN stage of cell plate formation. Both of these stages involve substantial cell plate growth, as is evidenced by the dramatic increase in surface area of the membranes (Figure 11). By contrast, no distinct CPAMs appear to encompass the cell plate membranes during the TN and the planar fenestrated sheet (PFS) stages, except over and around the large fenestrae of the PFSs that are being filled (Figures 9C and 9D). During both of these latter stages, the cell plate is remodeled but very little net membrane growth is observed (Figure 11).

The Initial Membrane Network of Cell Plates Is Formed from Dumbbell-Shaped Membrane Precursors

Dumbbell-shaped vesicles are frequently found within the CPAM of actively growing cell plates. Based on the different dumbbell morphologies observed in this study, they appear to arise from
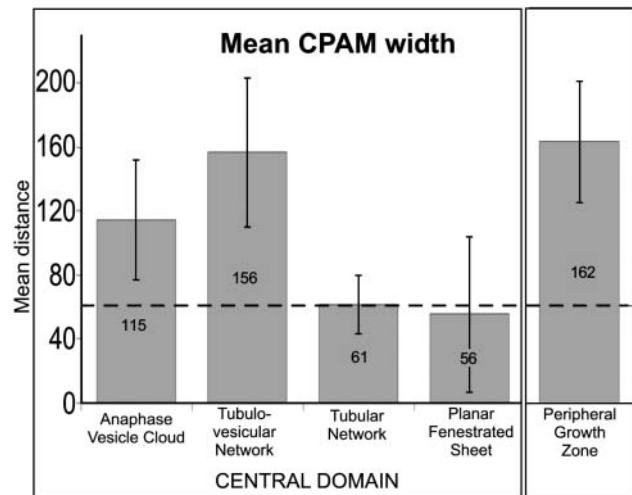

Figure 5. Changes in Width of the CPAM Associated with the Different Types of Cell Plates.

The mean distance ($\pm$SD) corresponds to the average distance between the cell plate and the closest 200 ribosomes. The dashed line marks the minimum threshold distance measured in stages in which no CPAM could be detected.

the stretching of the neck region of hourglass-shaped fused vesicles (Figures 6A to 6J). This neck region is initially marked by a band of darkly stained material, which upon careful 3-D analysis, resembles a ring-like collar (diameter ~38 nm; Figure 6B, inset) of variable length. Longer dumbbells frequently possess two collars, one adjacent to each bulbous end (Figures 6I and 6J), or lack collars entirely. Whereas some of the constricting collars exhibit a tight substructure, we have found several examples in which the collars exhibit an expanded spiral architecture (Figures 6E, 6K, and 6K', yellow arrows). Interestingly, in Figure 6E, only one of the two constricting rings exhibits an expanded spiral architecture. The expanded spiral shown in Figure 6K surrounds the narrow neck of a branching membrane structure within a TVN (e.g., Figure 6O). Because the tight collars shown here are similar to the Arabidopsis Dynamin-Like protein (ADL1)-type dynamin rings that constrict the wide tubules of forming endosperm cell plates (Otegui et al., 2001), we have tested the anti-ADL1 antibodies on our cell plates. The antibodies clearly labeled the cell plates at different stages (data not shown). However, the relatively poor structural preservation of the membranes in the Lowicryl-embedded specimens prevented us from unambiguously identifying the labeled structures as isolated dumbbells or TVN tubules.

The surface area of dumbbells (~15,000 nm^2) corresponds to the surface area of two small-dark vesicles (2$\times$ ~7100 nm^2) and of the fused hourglass structures (~14,500 nm^2; cf. Figures 6A and 6E). What changes during the stretching of the dumbbell necks is the diameter and surface area of the bulbous ends, which get smaller. The simultaneous reduction in dumbbell volume can amount to ~50% of the starting volume, and this volume reduction tends to be paralleled by an increase in staining density of the dumbbell contents (Figures 6E and 7C). Figures 6L
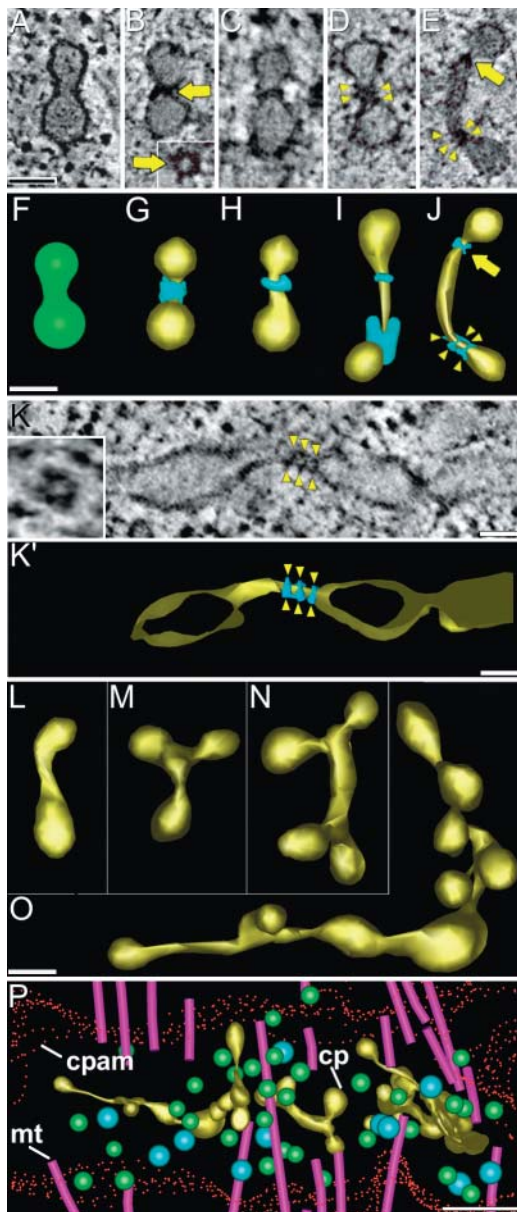
Figure 6. Formation of Dumbbell Vesicles from Freshly Fused Hourglass Vesicles and Initial Cell Plate Assembly Steps.

(A) to **(K′)** Tomographic slice **(A)** and model **(F)** of an hourglass-shaped vesicle fusion profile. Arrows point to compact dynamin-like springs; arrowheads point to individual loops of the expanded dynamin-like spring. Insets in **(B)** and **(K)**, tomographic face-on views of compact and dynamin-like springs, respectively.

(B) to **(E)** Tomographic slices of dumbbell vesicles with dynamin-like springs.

(G) to **(J)** Modeled dumbbell vesicles with dynamin-like springs at different stages during elongation.

(K) Tomographic image of a TVN-stage cell plate tubule with an expanded dynamin-like spring.

(K′) Model of K structures.

(L) to **(O)** Cell plate intermediates showing how the fusion of vesicles to the dumbbell ends gives rise to TVN-type cell plate networks.

to 6O illustrate the shapes of different membrane intermediates that appear to be derived from the fusion of additional vesicles to the bulbous ends of extended dumbbells. Such membrane structures are most frequently observed in early tubulo-vesicular stage cell plates (Figure 6P), a pattern consistent with the idea that they constitute the next stage of cell plate assembly.

The TVN Is Formed during the Solid Phragmoplast Stage of Cell Plate Formation

In Arabidopsis shoot and root meristem cells, the formation of the TVN (Figures 7A to 7E, see Supplemental Video Sequence 2 online) constitutes the major growth stage of cell plate assembly (Figure 11). This growth involves the delivery of large numbers of Golgi-derived vesicles to the cell plate. Because these vesicles appear to travel along phragmoplast MTs (Otegui et al., 2001; Liu et al., 2003), rapid cell plate formation requires large numbers of cell plate–associated MTs; hence the high density of MTs in the TVN-associated phragmoplast (Figure 7A, see Supplemental Video Sequence 2 online). Indeed, numerous vesicles are associated with the phragmoplast MTs of Figure 7A. However, some others apparently are not MT associated, and their mechanism of transport to the cell plate has yet to be clearly determined. During the TVN stage, the fusion of the incoming vesicles with the dumbbells gives rise to increasingly complex, branched membrane configurations (Figure 6O) that evolve into an ∼200-nm-thick TVN (Figures 7A and 7B). The fusion process is accompanied by an increase in staining of the luminal contents of the TVN compared with that of the cell plate–forming vesicles (Figures 7C and 7D).

The TVN membrane networks initially form island-like domains that subsequently join to form a coherent network across the width of the phragmoplast (Figures 7A and 7B). All of these cell plate assembly steps take place exclusively within a CPAM (Figures 4W, 7C, and 7E). During this stage of development, many of the new dumbbells seem to arise in physically separated CPAMs located close to the cell plate margins (Figure 7E). When these isolated CPAMs merge with the principal CPAM their dumbbells become part of the growing cell plate. Some cell plate structures that look like thin tubules in tomographic slices (Figure 7C, asterisk) actually correspond to small, thin, sheet-like domains (Figure 7B, asterisk), the very early precursors of planar sheets. The first clathrin-coated buds and vesicles also arise in association with late-stage TVN cell plates (Figure 7A). Abundant mitochondria (Figure 7A) surround the solid phragmoplast, whereas few ER tubules are observed (Figures 10A and 10B).

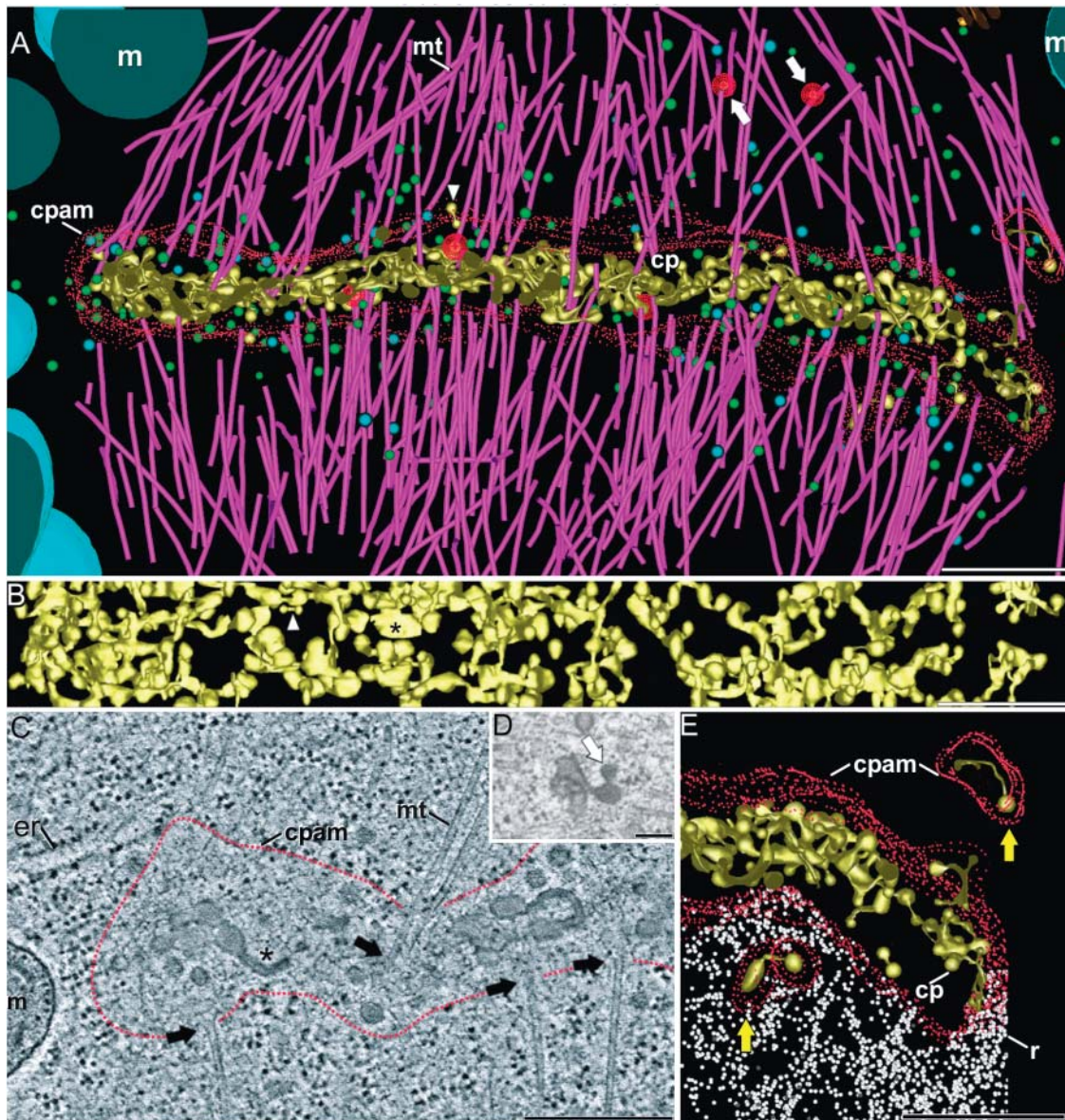### Transition to the TN Stage Coincides with the Loss of MTs and CPAM from the Central Region of the Phragmoplast

The transition from the TVN to the TN stage of cell plate formation involves a sudden loss of MTs and the disappearance of the

(P) An early TVN network consisting of isolated dumbbell-derived intermediates. cp, cell plate.

Bars in **(A)** to **(O)** = 50 nm; bar in **(P)** = 200 nm.

Figure 7. Solid Phragmoplast with CPAM and TVN Stage Cell Plate.

(A) Shoot apical meristem cell. Side view of a nearly complete TVN cell plate (cp) with its associated CPAM and phragmoplast MTs. Arrows point to clathrin-coated vesicles. Arrowhead points to a small dumbbell not yet integrated within the cell plate. m, mitochondria.

(B) Face-on view of the same TVN. Asterisk marks the initials of a future planar sheet region.

(C) Projection of 10 consecutive tomographic slices (2 nm thick each) through a TVN-type cell plate and its associated CPAM. Note that the MT (+) ends (arrows) terminate within the CPAM, where only very few ribosomes can occasionally be seen. The asterisk indicates a small thin sheet domain. m, mitochondria.

(D) Detail of a fusion profile (arrow) in a TVN-type cell plate showing the increased staining of the cell plate contents.

(E) Modeling of the ribosome-excluding CPAM. The ribosomes (r) define the outer boundary of the cocoon-like CPAM, which encompasses the TVN-type cell plate (cp). Isolated dumbbells (arrows) also are surrounded by a CPAM.

Bars in **(A)**, **(B)**, and **(E)** = 500 nm; bar in **(C)** = 200 nm; bar in **(D)** = 50 nm.

CPAM from the central region of the phragmoplast (Figures 8A and 8B, see Supplemental Video Sequence 3 online). Both of these changes mark the end of the rapid membrane growth phase within the solid phragmoplast. As CPAM and MT assembly shifts to the edge regions of the cell plate, so does the site of further cell plate growth and expansion. The central region of the cell plate, in turn, enters a phase of maturation that is evidenced by a decrease in cell plate–associated vesicles, changes in geometry of the cell plate membranes, the absence of dumbbell-shaped vesicles, and the appearance of large numbers of clathrin-coated buds and vesicles (Figures 8A to 8D, see Supplemental Video Sequence 3 online). First, the tubulo-vesicular membranes are converted into an anastomosing network of tubules (Figure 8C), and as the tubules widen, the network is transformed into a PFS (Figures 8D, 9C, and 9D). The central region of the phragmoplast associated with the tubular membrane network still contains some MTs but they end somewhat farther away from the cell plate surface and do not terminate in a CPAM (cf. Figures 7C and 8A). The loss of the CPAM is documented in Figure 8A, where ribosomes can be seen in close proximity to the cell plate membranes as well as in larger channels that traverse the cell plate (brackets).

In contrast with the homogenous, darkly stained TVN-type cell plates (Figures 7C and 7D), the TN-type cell plates appear more heterogeneous, with the narrower domains being darkly stained and the wider domains more lightly stained (Figure 8A). The lighter stained cell plate domains (Figure 8A, arrows) correspond to sites of callose deposition (immunolabeling data not shown), as reported by Samuels et al. (1995).

Centrifugal Cell Plate Growth and the Filling of Large Fenestrated Sheet Openings Involve CPAMs and Associated MTs

During the final phase of cell plate formation, centrifugal growth in the peripheral growth zone (PGZ) leads to the fusion of the cell plate with the mother cell wall. Simultaneously, localized growth confined to the large fenestrae leads to the closing of these cell plate holes and to the completion of the new wall. Both of these processes occur within secondary CPAMs to which MTs are attached (Figures 9A and 9C to 9E). By contrast, the completed cell plate regions are devoid of CPAMs and associated MTs, which allows Golgi stacks and mitochondria to accumulate close by (Figures 9A and 9C, see Supplemental Video Sequence 4 online). Many clathrin-coated buds and vesicles are seen in the more mature PFS cell plate region (Figures 9A to 9C). The mature buds exhibit a collar-like structure around their constricted necks (Figure 9B). These collars exhibit a dynamin spring-like substructure like those shown in Figures 6A to 6E.

The PGZ can be distinguished from the central zone on the basis of temporal and structural criteria. Temporally, it arises only after the central TVN-type cell plate has been completed and the solid phragmoplast is replaced by the ring-shaped phragmoplast. Structurally, it is defined by a ring-like CPAM within which the MT (+) ends are embedded and by a mixture of the above-described cell plate geometries, caused by the nonuniform

pattern of centrifugal growth. In some EM micrographs of whole cell plates, opposite PGZs showed an asymmetric pattern of growth, with one side already fused to the plasma membrane, whereas the other side was not (data not shown).

The termination of the PGZ MTs at the edge of the CPAM is shown in Figure 9A. Other clusters of MTs are seen to focus on the large fenestrae that possess CPAM coats (Figure 9D). The MT-rich PGZ also contains a high density of vesicles (Figures 9C to 9E). At this stage of development, the number of small-dark (green) vesicles is similar to the number of large-light (blue) vesicles (Figure 3). The island-like disposition of CPAM regions over large fenestrae and the sheet-like organization of the CPAM over the PGZ are illustrated in Figures 9D and 9E, together with the higher concentration of vesicles within the CPAMs.

The Spatial Organization of the ER Changes during Each Stage of Cell Plate Assembly

It has been postulated that the ER plays a significant role in plant cytokinesis, given the intimate ER–cell plate associations shown in electron micrographs of cells preserved by chemical fixation and stained with osmium ferricyanide (Hepler, 1982). Here, we document the spatial organization of the cell plate–associated ER membranes in Arabidopsis meristem cells preserved by high-pressure freezing/freeze substitution techniques. As illustrated in Figures 1 and 10, the number of ER membranes that interact with the forming cell plate increases over time, and the associations become both more complex and more intimate.

During late anaphase, when the first vesicle clouds become surrounded by CPAMs (Figures 1B and 1C), the ER is oriented parallel to the MTs. The sparse ER membranes do not show any specific association with the forming cell plate region. Indeed, they appear to be excluded from the CPAM regions associated with the phragmoplast initials (Figure 1C). Only after the initial CPAMs have expanded into a coherent, equatorial compartment with a tubulo-vesicular cell plate core are a few trapped ER cisternae seen crossing the CPAM region (Figure 10A). Where they pass through the TVN, the ER cisternae appear highly branched and tubular, giving rise to clusters of thin ER tubules (Figures 10A and 10B). On either side of the cell plate, these irregular ER tubules merge into wider tubules that extend along the phragmoplast MTs away from the cell plate. Between the ER-containing domains there are large cell plate regions that are devoid of ER membranes. The ER membranes that cross the outermost regions of the tubulo-vesicular cell plates tend to form wider tubules but are also oriented parallel to the MTs (Figure 10A).

During the TN stage, the amount of cell plate–associated ER continues to increase (data not shown), reaching a maximum during the fenestrated sheet stage of development. During the latter stage, the cell plate becomes evenly covered by a network of tubular ER membranes (Figures 10C and 10D), many of which appear to be physically linked to the cell plate by evenly spaced small anchoring structures (Figure 10E). At this stage, the ER tubules that cross the cell plate are seen to pass through the fenestrae. The ER membranes in the PGZ exhibit a more loose association with the cell plate (Figure 10C).
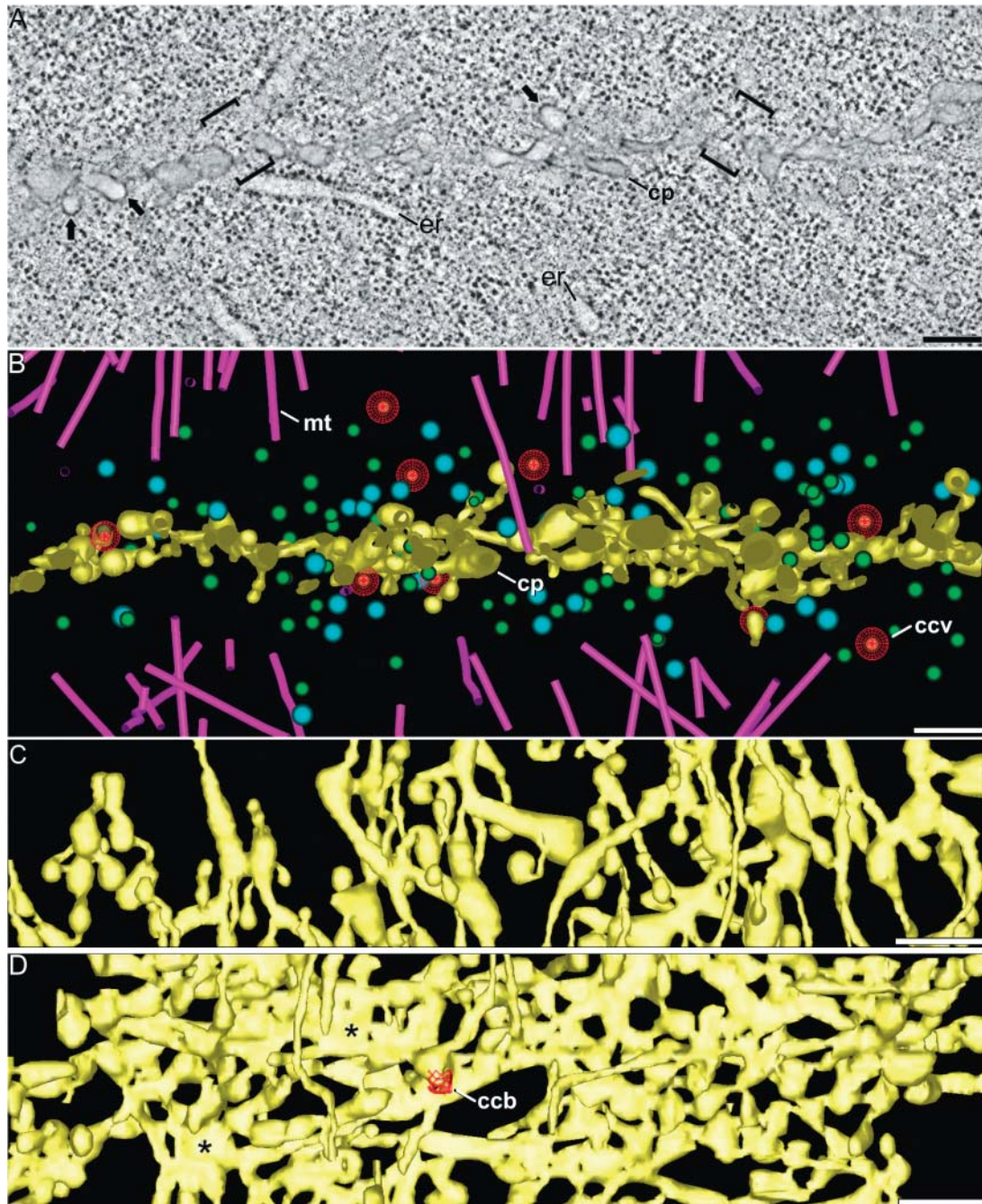
Figure 8. TN Stage Cell Plates.

(A) and **(D)** Shoot apical meristematic cell.
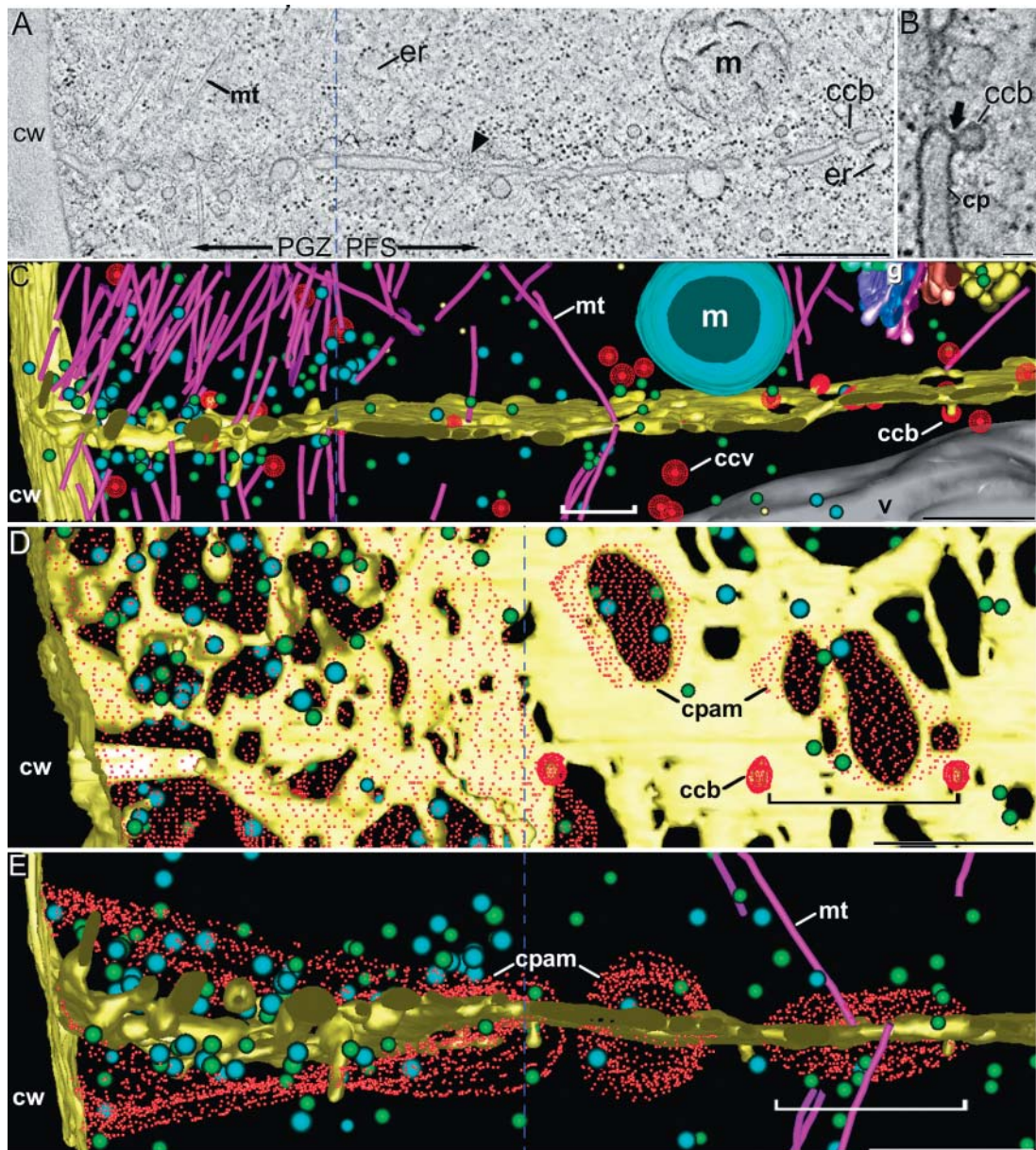**(B)** and **(C)** Root meristematic cell.
(A) Tomographic slice of a TN. Arrows point to sites of early callose accumulation. Note the absence of a CPAM around a cell plate (cp) as evidenced by *trans* cell plate channels (delineated with brackets) filled with ribosomes.
(B) Note the lower density of MTs compared with the TVN stage (Figure 7A) and their greater separation from the cell plate. ccv, clathrin-coated vesicles; cp, cell plate.
(C) and **(D)** Face-on views of modeled early and late TN-type cell plates. The callose-induced tubule widening leads to increasingly large planar fenestrated domains (asterisks). ccb, clathrin-coated buds; ccv, clathrin-coated vesicles.
Bars = 200 nm.

Figure 9. Tomographic Images of the PGZ and the PFS Cell Plates.

Tomographic images ([**A**] and [**B**]) and models ([**C**] to [**E**]) of half of a PGZ/PFS cell plate.
(A) Shoot apical meristematic cell. The leftmost part of the cell plate (PGZ) is still actively growing and exhibits a mixture of features typical of TVN and TN stage cell plates. The PFS lacks a CPAM except over large fenestra (arrowhead). ccb, clathrin-coated buds; cw, cell wall; m, mitochondria.
**(B)** Detail of a PFS cell plate region (cp) where a dense dynamin-like ring (arrow) is found constricting a clathrin-coated bud (ccb).
(C) Side model view of the PGZ and PFS regions. Note the convergence of MTs and vesicles over the PGZ region and the high density of clathrin-coated buds (ccb) and vesicles (ccv) over the PFS. cw, cell wall; g, Golgi stack; m, mitochondria; v, vesicle.
(D) and **(E)** CPAMs are seen to encompass the PGZ region and to cover individual fenestrae of the PFS. Note the focusing of MTs to the CPAM regions where the MT (+) ends are embedded. Brackets mark the same fenestrae in **(C)** to **(E)**. ccb, clatrin-coated bud; cw, cell wall.
Bars in **(A)** and in **(C)** to **(E)** = 500 nm; bar in **(B)** = 50 nm.
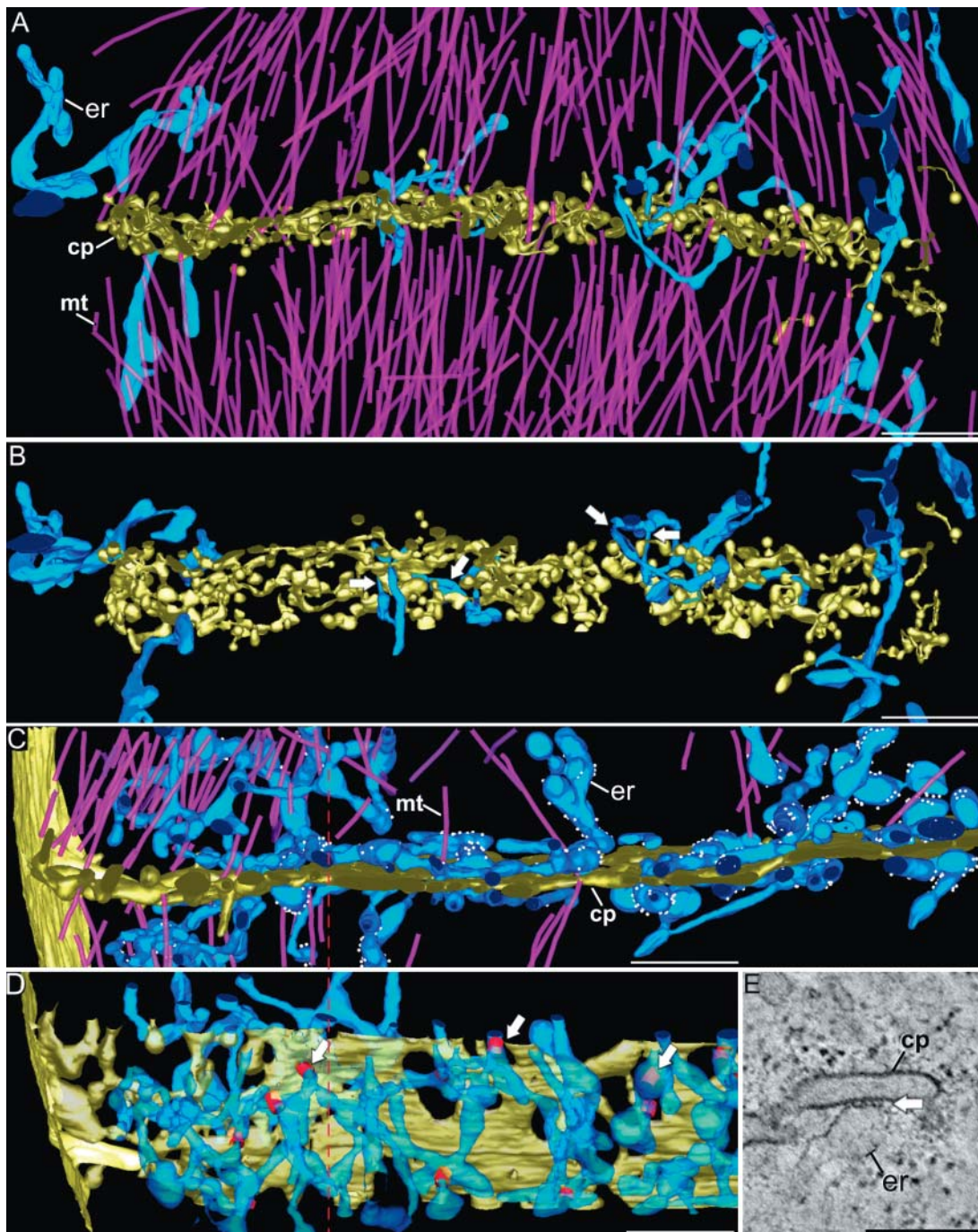
Figure 10. Changes in the Organization of the ER during Cell Plate Formation.

(A) and **(B)** TVN stage.

(A) Side view of the cell plate (cp). Note the limited number of sites where ER–TVN cell plate interaction occurs. Similarly, few ER cisternae are seen between the solid phragmoplast MTs.

(B) 45° tilt view of the TVN shown in **(A)**. At the cell plate surface the ER cisternae branch, giving rise to very narrow ER tubules that cross the cell plate (arrows).

(C) and **(D)** Association of ER membranes with PGZ and PFS cell plate regions. Dashed line marks the transition between them.

(C) Side view. Many cytoplasmic ER tubules are seen intermingled with MTs over the PGZ region (left side), but little direct interaction of ER tubules with cell plate (cp) membranes is observed. By contrast, in the PFS zone (right), numerous ER tubules appear closely associated with the cell plate. Small white spheres correspond to ER-bound ribosomes.

Quantitative Analysis of the Cell Plate Intermediates Provides Insights into Cell Plate–Associated Vesicle Trafficking

To better understand the cell plate assembly and transformation processes described in the preceding sections, we have calculated the changes in surface area and volume of the different cell plate intermediates (Figure 11). For each stage, we calculated the average cell plate membrane surface area and cell plate volume contained in 1-μm^3 boxes taken from different central cell plate regions of different tomograms (see Methods). Because the cell plate is built from Golgi-derived vesicles (small-dark and large-light) and the removal of excess membrane involves clathrin-coated vesicles, we have expressed the surface and volume changes in terms of vesicle equivalents. Because each large-light vesicle appears to arise from the fusion of two small-dark vesicles before they arrive at the cell plate assembly site, we have expressed all cell plate growth in equivalents of the small-dark vesicle ($\sim$51 nm in diameter), the type of vesicle produced by the Golgi stacks. Note that our data are derived from static samples. For this reason, the vesicle numbers reflect only net surface and volume changes and not total numbers of vesicles needed to produce the different cell plate networks.

The principal phase of cell plate growth in Arabidopsis meristematic cells coincides with the assembly of the TVN by the solid phragmoplast (Figure 11). To create the TVN-type cell plate surface area (2.4 μm^2) contained in 1 μm^3 of cell volume (Figures 7A and 7B) requires $\sim$338 small-dark vesicle equivalents. During the following transformation of the TVN to a TN-type cell plate (Figures 8B to 8D), the net increase in surface area is an additional 0.4 μm^2, which implies 48 small vesicle equivalents. A reduction in surface area by 1 μm^2/μm^3, or $\sim$181 clathrin-coated vesicle equivalents, is observed during the transformation of the TN to a PFS-type of cell plate (Figures 9B and 9C).

An interesting discrepancy is seen between the number of small-dark vesicle equivalents needed to produce the surface area of the TVN-type of cell plate and the number of small vesicle equivalents required to produce the TVN volume. Thus, whereas the TVN surface area corresponds to $\sim$338 vesicle equivalents per 1 μm^3 box, the volume corresponds to only $\sim$107 vesicle equivalents (Figure 11). This suggests that during TVN formation, the volume of the resulting network is reduced $\sim$70%. In parallel, an increase in staining of the luminal contents of the TVN compartments compared with the cell plate–forming vesicles (Figures 7C and 7D) is observed. On the other hand, the proportionally greater increases in cell plate volume during the transformation of the TVN to a TN and of the TN to a PFS-type cell plate appear to be caused by the accumulation of callose, which is made by cell plate–associated enzymes (Verma, 2001).

Because the PGZ does not mature uniformly, we could not derive any meaningful data for its surface area and volume.

DISCUSSION

We have used a combination of cryofixation/freeze-substitution and electron tomography techniques to reevaluate the mechanism of somatic-type cell plate assembly in Arabidopsis. Aside from providing more detailed qualitative and quantitative information on the cell plate membrane networks previously described by Samuels et al. (1995) and Rensing et al. (2002), our tomograms have yielded the following findings. (1) Cell plate vesicle fusion and dumbbell formation start in phragmoplast initials, which are formed by clusters of residual polar MTs. (2) Cell plate growth is limited to specialized, ribosome-excluding cytoplasmic domains termed CPAMs. (3) Virtually all (+) ends of the phragmoplast MTs end within CPAMs. (4) Cell plate–forming vesicles on their way to the cell plate carry L-shaped appendages, putative precursors of exocyst-type tethering molecules, but only inside the CPAMs are vesicle pairs connected by Y-shaped complexes seen. (5) Cell plate assembly appears to start with the transformation of hourglass-shaped vesicle fusion intermediates into extended dumbbell-shaped vesicles by means of dynamin-like protein spirals that undergo conformational changes. (6) Dumbbell formation decreases vesicle volume by 50%. (7) Transformation of the dumbbells into a TVN occurs in a uniform manner across the entire width of the solid phragmoplast. (8) Upon completion of the TVN, the CPAM and the MTs break down and then reassemble along the TVN margin into a ring phragmoplast to create the PGZ. (9) CPAM breakdown precedes the maturation of the TVN into a cell wall.

Somatic-Type Cytokinesis Can Be Divided into Four Phases According to the Organization of the CPAM and Associated MTs

Given the results of this study as well as the findings of others (Hepler and Newcomb, 1967; Bajer, 1968; Gunning, 1982; Valster et al., 1997; Nacry et al., 2000; Verma, 2001), we have formulated a model of somatic-type cell cytokinesis that distinguishes four phases. Phase I coincides with the process of phragmoplast assembly during late anaphase. During this phase, clusters of residual polar spindle MTs appear to serve as initial scaffoldings for bringing both cell plate–forming vesicles and CPAM components to the site of cell plate assembly (Figures 1 and 12). The first dumbbells arise between vesicles within these very early CPAM domains. Lateral expansion and coalescence of the original CPAM domains and their MTs lead to the solid type of phragmoplast MT array (Figure 7A).

Figure 10. (continued).

(D) 45° tilt view of **(C)**. For better viewing of the numerous cell plate–crossing tubular ER regions, the corresponding membrane domains have been highlighted with a red collar (arrows), and the top layer of ER membranes is displayed in a semitransparent mode.

(E) Detail of a contact site (arrow) between an ER tubule and a PFS-type cell plate (cp). Note the membrane-bridging elements.

Bars in **(A)** to **(D)** = 500 nm; bar in **(E)** = 200 nm.

A   Unit central cell plate surface area

B   Unit central cell plate volume
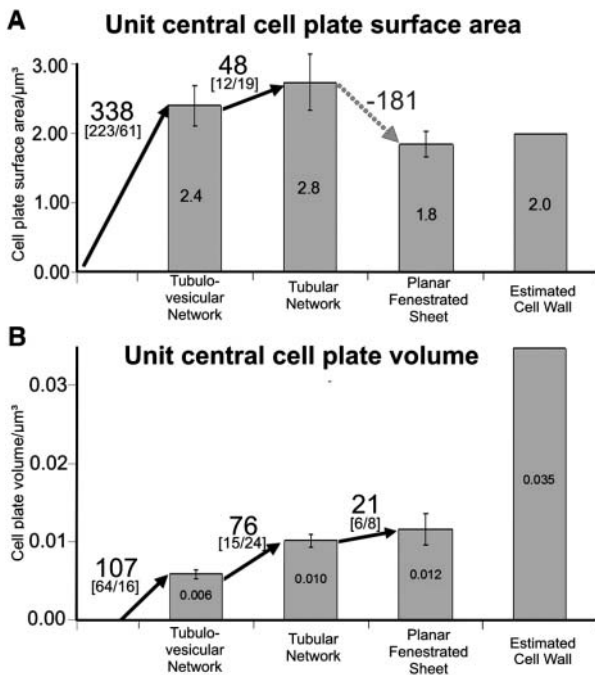
Figure 11. Changes in Cell Plate Surface Area and Volume during Different Stages of Somatic-Type Cell Plate Formation.

The numbers in the bars indicate the mean cell plate surface area **(A)** and volume **(B)** per 1 $\mu m^3 \pm$ SD, and the numbers next to the black arrows reflect the net growth unit cell plate surface area **(A)** or volume **(B)** in terms of small vesicle equivalents. The bracketed numbers reflect the predicted numbers of small/large (in black/gray, respectively) vesicle equivalents required for these changes given the vesicle ratios documented in Figure 3. The gray dotted arrow indicates net loss changes in cell plate surface area in terms of clathrin-coated vesicle equivalents. As a reference, the estimated final cell wall surface area and volume values also are displayed.

During phase II, all of the cell plate assembly processes take place within the CPAM, which occupies the equatorial plane of the solid phragmoplast (Figures 7A and 12). During this phase, the CPAM forms a flat, cocoon-like structure within which the (+) ends of the MTs terminate. The diameter of the CPAM always corresponds to the diameter of the solid phragmoplast. Growth of the TVN-type cell plate occurs across the entire width of the CPAM (Figure 12).

Phase III marks the transition from cell plate assembly to maturation. The central, TVN-encompassing CPAM and associated solid phragmoplast MTs break down (Figure 8A), whereas new MTs and a new CPAM assemble in the cell plate periphery, giving rise to the new ring phragmoplast and PGZ (Figure 12). In the central region, the CPAM-free cell plate is converted to a flattened TN by callose deposition.

During phase IV, the central cell plate region undergoes a series of maturation steps that require little membrane growth (Figure 11) and converts into a CPAM-free, planar sheet with several open fenestrae. Secondary CPAMs and associated MTs assemble around the big fenestrae to close them with more arriving vesicles (Figure 9). The PGZ (Figures 9 and 12) expands

centrifugally in a phase of uneven cell plate growth and maturation that eventually leads to the fusion of the cell plate with the mother cell walls.

The CPAM Defines the Distribution of Phragmoplast MTs and the Sites of Cell Plate Growth

The presence of an ill-defined dense matrix material around the growing cell plate, where the proximal ends of MTs terminate, was already suggested by Gunning (1982). In 1995, Samuels et al. described a fine filamentous and ribosome-excluding cytoplasmic matrix associated with the TVN stage of cell plate assembly in *Nicotiana tabacum* (tobacco) BY-2 cells. Subsequent studies of syncytial-type cell plates (Otegui et al., 2001; Otegui and Staehelin, 2004) have shown that a similar matrix surrounds the growing wide TNs in cellularizing endosperm and microsporocytes of Arabidopsis. These authors also demonstrated an association of this matrix with tethered vesicles and MTs and provided evidence for the matrix components being delivered together with vesicles to the cell plate region. Because of these findings, this ribosome-excluding matrix was termed a CPAM (Otegui and Staehelin, 2004). The current investigation has demonstrated that the CPAM of somatic-type cell plates possesses all of these attributes, while also providing evidence for its role in cell plate assembly.

Although the relationship between the (+) ends of the phragmoplast MTs and the CPAM has yet to be described in molecular terms, the following findings of others indicate that the phragmoplast MTs not only terminate within the CPAM but could be physically linked to this matrix. Thus, as shown by Kakimoto and Shibaoka (1992), it is possible to isolate intact phragmoplasts (cell plates with opposing sets of phragmoplast MTs) from synchronized, dividing *N. tabacum* BY-2 cells. To survive the mechanical shearing forces associated with cell disruption and purification, the phragmoplast MTs must be attached to cell plate–associated structures, presumably CPAM molecules. Actomyosin systems also play a role in positioning the cell plate within the plane of division (Hepler et al., 2002). When this positioning is altered by myosin-disrupting agents, both the cell plate and its associated MTs and actin filaments become misaligned as a unit (Molchan et al., 2002).

Because the cell plate–forming vesicles travel along MTs to the cell plate (Otegui et al., 2001; Molchan et al., 2002), the termination of the MT (+) ends within the CPAM would appear to be functionally important. First, it could stabilize the (+) ends of the attached MTs and thereby increase the half-life of those MTs with which the CPAM can establish a functional relationship. Recently, a number of MT (+) end binding proteins have been characterized in other systems (Carvalho et al., 2003), but none of these proteins have yet been localized to cell plates. A second important function of the MT–CPAM association is that it ensures that cell plate–forming vesicles are preferentially delivered to the CPAM and thereby to the cell plate and not to other cellular destinations. For these reasons, we propose that the definition of the phragmoplast be extended to include the CPAM in addition to MTs and actin filaments.

The most compelling observation to support the hypothesis that the CPAM actually controls the vesicle fusion events that
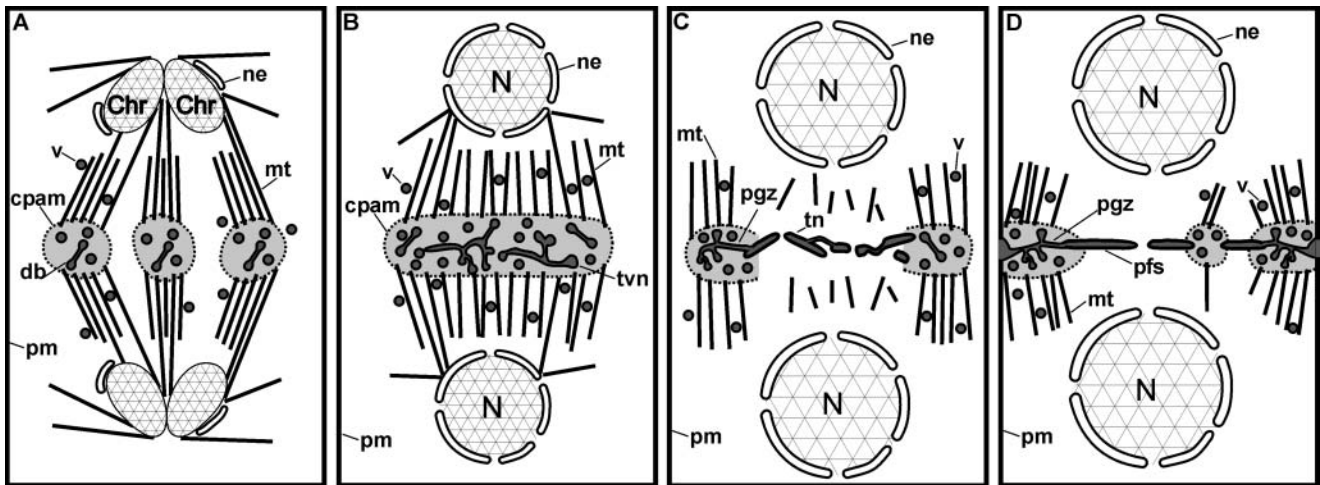
Figure 12. Model of Plant Somatic-Type Cytokinesis.

(A) Phragmoplast assembly phase during late anaphase. Phragmoplast initials arise from opposite sets of polar spindle MTs. Vesicles (v) travel along MTs toward the assembly sites, defined by the presence of CPAMs. Inside the CPAMs, the first cell plate initials are produced through the formation of dumbbell-shaped (db) vesicle intermediates (see also Figure 13). Chr, chromosomes; ne, nuclear envelope; pm, plasma membrane.

(B) Solid phragmoplast phase. After fusion of vesicles to the dumbbell ends and joining of the enlarged phragmoplast initials, a TVN cell plate arises within the CPAM that now extends across the entire interzone between the two sets of opposing MTs that form the solid phragmoplast. N, nucleus; ne, nuclear envelope; pm, plasma membrane; v, vesicles.

(C) Transitional phragmoplast phase. As the central CPAM and associated MTs disassemble, a new CPAM with MTs arises at the edge of the cell plate, giving rise to the ring-shaped phragmoplast and the PGZ. In parallel, the TVN cell plate is converted into a TN through callose synthesis in the cell plate lumen. N, nucleus; ne, nuclear envelope; pm, plasma membrane; v, vesicles.

(D) Ring-shaped phragmoplast phase. As the central cell plate domain is converted to a PFS, secondary CPAMs and associated MTs reform over the remaining large fenestrae, focusing cell plate growth to these regions. The ring-shaped phragmoplast and CPAM define the PGZ, which expands centrifugally until the cell plate reaches and fuses with the plasma membrane (pm). N, nucleus; ne, nuclear envelope; pm, plasma membrane; v, vesicles.

lead to cell plate formation is the finding that dumbbell-shaped vesicles, the structures that nucleate cell plate growth, are produced only inside CPAMs (Figures 1C, 6P, and 7E). The confinement of tethered vesicle structures to the CPAM regions suggests that the CPAM may play a role in the formation of vesicle tethers (see below) and/or stabilize the tethered vesicle configuration.

Cell Plate–Forming Vesicles Become Tethered by Putative Exocyst-Like Complexes before Fusion with Other Vesicles or with Growing Cell Plate Domains

It is now well established that the process of vesicle fusion requires several protein complexes, both to ensure specificity of membrane docking and to mediate membrane fusion. Whereas SNAREs have been shown to control the membrane fusion events (Lauber et al., 1997; Sanderfoot et al., 2000; Waizenegger et al., 2000; Guertin et al., 2002), tethering complexes are used to impart specificity (Guo et al., 2001). The tethering complexes employed in polarized exocytosis in both yeast and mammalian cells are known as exocyst complexes in yeast and sec6/8 complexes in mammals (TerBush et al., 1996, 2001; Hsu et al., 1998, 1999). Assembly of a functional tethering complex involves the recruitment of several subunits to vesicles and, in parallel, recruitment of another subunit (Sec3 in yeasts and Exo70 in mammals) to the target membranes (Finger et al., 1998; Matern et al., 2001).

Cell plate formation in plants can be viewed as constituting a special type of polarized exocytosis. In plant syncytial-type cytokinesis, tethering structures have been shown to connect cell plate–forming vesicles (Otegui and Staehelin, 2004), and it was speculated that these structures could correspond to exocyst-like complexes. The recent identification of several putative exocyst subunits in the Arabidopsis genome (AtSec5, AtSec6, AtSec15, AtExo70, and AtExo84, Cvrckova et al., 2001; AtSec3, J.M. Seguí-Simarro and L.A. Staehelin, unpublished results) lends further support to this notion. Our data suggest that the vesicles used for somatic-type cell plate formation become tethered within the CPAM before fusion and that these tethering complexes are very similar in geometry and length to the exocyst complexes isolated from rat brain (Hsu et al., 1998).

The same vesicles that carry exocyst-like tethering complexes also carry L-shaped complexes (Figures 4I to 4P). This finding, together with the fact that the L- and Y-shaped complexes have the same length (∼35 nm) and exhibit a related morphology (L-shaped complexes lack one short arm), suggests that the L-shaped molecules are precursor forms of plant exocyst-like complexes that lack one or several subunits.

In yeasts and mammals, actin microfilaments and Rho and Rab GTPases are required for the regulation of the exocyst complex (Hsu et al., 1999; Guo et al., 2001; Lipschutz and Mostov, 2002). Consistent with this hypothesis, both Rops (Rho-related GTPases of plants) and short actin microfilaments (reviewed in Bednarek and Falbel, 2002), together with putative

plant exocyst-like complexes (this study), have been found associated with the cell plates/CPAMs during cytokinesis. Given these findings, we propose that recruitment of putative plant exocyst-like complex subunits other than AtSec3 to cell plate–forming vesicles outside the CPAM gives rise to the L-shaped complexes (Figure 13). By contrast, conditions within the CPAM might promote binding of AtSec3 to the target membrane (Hsu et al., 1999) and thereby formation of the Y-shaped exocyst-like tethering complexes.

The Formation of Dumbbell-Shaped Vesicles with a Reduced Volume Appears to Involve Expanding Dynamin-Like Spirals

Dynamin-GTPases are mechanoenzymes that constrict and fission membrane vesicles and tubules containing phosphatidy-linositol-4, 5 bisphosphate lipids (Stowell et al., 1999). Dynamin-like proteins have been identified in mammalian, fungal, and plant cells (van der Bliek, 1999). In plants, several dynamin homologs have been localized to somatic-type cell plates, including *Glycine max* (soybean) phragmoplastin (Gu and Verma, 1996, 1997) and the Arabidopsis homologs ADL1A and ADLH (Lauber et al., 1997; Kang et al., 2001, 2003). These dynamins have been postulated to be responsible for producing the dumbbell-shaped vesicles of somatic-type cell plates (Samuels

Figure 13. Hypothetical Model Explaining How Golgi-Derived, Cell Plate–Forming Vesicles Can Give Rise to Large Vesicles and to Dumbbells.

Small, Golgi-derived vesicles outside the CPAM interact through an unknown tethering complex before fusion and give rise to large-light vesicles. Vesicles that enter the CPAM before fusion first become tethered through an exocyst-like complex and then give rise to an hourglass intermediate. This hourglass-type vesicle is converted into a dumbbell vesicle with the help of dynamin springs. First, GTP-dynamin monomers are assembled into tight springs around the hourglass vesicle necks. GTP hydrolysis causes expansion of the dynamin spring, which elongates the neck to form a dumbbell. New GTP-dynamin springs are assembled next to the bulbous ends of the dumbbell, and the expansion/stretching process is repeated. During each neck elongation step, the volume of the vesicle is reduced by expulsion of water. The resulting concentration of the vesicle contents (pectic polysaccharides and xyloglucans) could lead to polysaccharide gelling and thereby stabilize the elongated vesicle architecture.

et al., 1995; Verma, 2001). ADL1A-type dynamin rings and spirals also have been shown to transiently constrict the tubules of wide TNs in cellularizing Arabidopsis endosperm cells (Otegui et al., 2001).
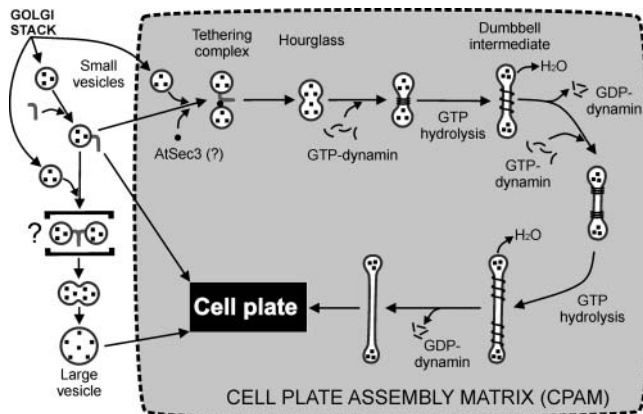
The tomographic data of this study provide evidence that dynamin-like molecules are involved in two different cell plate activities, the formation of dumbbells (Figures 6A to 6J) and the production of clathrin-coated vesicles that remove membrane from the maturing cell plates (Figure 9B). Our results also provide in situ support of the hypothesis advanced by Stowell et al. (1999) and Marks et al. (2001) that dynamin-like spirals elongate membrane tubules by undergoing a conformational change that induces a spring-like expansion. The expansion (relaxation) of membrane-associated dynamin springs is driven by the hydro-lysis of dynamin-bound GTP. The energy released in this reaction is sufficient to shear the neck region of clathrin-coated buds, whose rigid coat prevents the vesicle membrane from stretching to accommodate the dynamin-induced squeezing force.

In contrast with clathrin-coated buds, the bulbous ends of the dumbbell-shaped vesicles are not covered by rigid coats. Thus, when the dynamin-like springs expand, the membranes sur-rounding the bulbous ends can stretch transiently to accommo-date the fluids that are propelled into those ends. This short-lived membrane stretching (Fu et al., 2000) would be expected to increase membrane permeability, allowing water but not the cell plate–forming polysaccharides to exit to alleviate the pressure. We have found that the formation of dumbbells involves a decrease in vesicle volume by up to 50% with no change in membrane surface area. Formation of the long dumbbells ap-pears to require multiple rounds of dynamin-like spring assem-bly, expansion, and breakdown (Figures 6E, 6G, and 6J). The presence of dynamin-like springs on tubules of TVN-stage cell plates (Figures 6K and 6K′) suggests that this cell plate volume reduction mechanism continues to operate after the dumbbells have been incorporated into the TVN. Indeed, during assembly of the TVN, the cell plate contents appear to undergo an ∼70% reduction in volume compared with the originating vesicles (Figure 11).

Although hourglass-shaped vesicle fusion intermediates are seen outside the CPAM, those vesicles never seem to be converted into dumbbells. Instead, they appear to give rise to the class of large-light vesicles, whose surface area is twice that of the small-dark vesicles produced by the Golgi (Figure 13). Dividing plant cells have been reported previously to contain both dense and light vesicles (Hepler and Newcomb, 1967; Mollenhauer and Mollenhauer, 1976).

Reduction of Vesicle Volume during Dumbbell Formation May Cause Gelling of Cell Plate–Forming Polysaccharides

Why are dumbbell-shaped vesicles produced during somatic-type cell plate formation, and why do the dumbbells maintain their shape after loss of the constricting dynamin springs? Considering the number of mechanoenzymes and related pro-teins devoted to the production of dumbbell-shaped vesicles, this process must be of critical importance to cell plate formation. Here, we postulate that the primary function of this process is to

concentrate the vesicle contents to induce gelling of the cell plate–forming polysaccharides.

The Golgi-derived vesicles that give rise to cell plates and cell walls contain pectic polysaccharides, hemicelluloses, and arabinogalactan proteins (Staehelin and Moore, 1995). Pectic polysaccharides, in particular, are well-known gelling agents. Highly esterified pectins form gels through hydrophobic interactions, whereas low-esterified pectins form Ca^{2+}-pectate gels (Thakur et al., 1997). Because the Golgi produces highly methyl-esterified pectic polysaccharides (Zhang and Staehelin, 1992) that are later de-esterified by cell wall–localized esterases (Goldberg et al., 1996), it is likely that the dumbbell vesicles contain primarily esterified pectins. Removal of water from such vesicles would facilitate hydrophobic interactions that, together with a number of other factors (Thakur et al., 1997), would be expected to induce the formation of a hydrophobic-type gel. Gels can maintain their shape over extended periods of time because they present an elastic structure that does not readily rearrange (Rees, 1977). Thus, the primary function of dumbbell formation would be to create mechanically stable, elongated cell plate–forming vesicle intermediates. We speculate that during later stages of cell plate assembly, maintenance of the planar cell plate architecture is mediated by a combination of mechanical and vesicle-collapsing osmotic forces.

The formation of dumbbells also may aid the formation of two-dimensional cell plate networks from vesicles. To this end, the constriction of the waist regions of the dumbbells could serve to prevent the ballooning of vesicles, both creating stable, elongated cell plate building blocks and focusing the fusion of new vesicles to the dumbbell ends by displacing the fusion-initiating proteins such as knolle and keule (Waizenegger et al., 2000) to these ends.

Breakdown of the CPAM and MTs of the Solid Phragmoplast Coincide with the Initiation of Cell Plate Maturation and Assembly of the Ring Phragmoplast

Growth of the TVN and subsequent maturation into a TN occurs in a synchronized manner across the entire width of the cell plate (Figures 7A and 8B). The triggering event for this maturation is unknown but may be the same signal that initiates the breakdown of the CPAM and associated MTs. The next step, the transformation of the TN into a PFS, involves activation of callose synthases in the cell plate membrane (Samuels et al., 1995; Verma, 2001). Callose deposits, initially confined to a limited number of tubules, appear to provide the driving force for swelling the thin tubules into wider tubules and then expanding them into fenestrated sheets. The increase over time of the proportion of wide tubules is followed by the appearance of the first small fenestrated sheet domains (Figure 8D), which expand into the PFS. The surface area present in the TN cell plate suffices for a final cell wall (Figure 11A), indicating that very little net cell plate growth occurs in the absence of a CPAM.

In Arabidopsis meristematic cells, the PGZ first formed by the transitional phragmoplast is rather narrow (Figures 9A and 9B). Within this zone, centrifugal growth is irregular. This leads to an uneven pattern of maturation, with TVN- and TN-type domains juxtaposed to fenestrated sheet domains (Figure 9C). This irregular pattern of growth may explain why in some cases we observed the PGZ already linked to the plasma membrane on one side but not on the other. This asymmetric appearance of the cell plate is consistent with observations in other studies (Cutler and Ehrhardt, 2002; Ueda et al., 2003). The PGZ is embedded in a prominent CPAM. In the adjacent PFS domains, secondary CPAM patches with attached MTs are seen to form over large fenestrae, presumably to orchestrate the growth needed to close these cell plate holes. In parallel, there is a significant removal of surface area (Figure 11A), a process that involves formation of clathrin-coated vesicles (Figures 9A and 9B; Samuels et al., 1995).

The Organization of the Cell Plate–Associated ER Changes with the Cell Plate Phase

The association of ER membranes with somatic-type cell plates has been known for many years (Hepler and Newcomb, 1967). Because cell plates contain elevated concentrations of Ca^{2+} and the ER is assumed to regulate local Ca^{2+} levels, knowledge of the organization of the ER during the different phases of cell plate assembly is important. Ca^{2+} is known to regulate a number of activities related to cell plate formation, including membrane fusion (Hepler et al., 1990, 1994), the dynamics of cytoskeletal elements (Hepler et al., 1990), cell plate callose synthase activity (Kakimoto and Shibaoka, 1992; Verma and Hong, 2001), and dynamin dynamics (Verma, 2001).

Several studies of dividing meristematic cells (Hepler and Newcomb, 1967; Hepler, 1982; Schopfer and Hepler, 1991) and pollen grains (Brown and Lemmon, 1991, 1992) have reported that extensive ER networks form intricate associations with the vesicles involved in cell plate growth, starting with the earliest stages of cell plate formation. In light of these earlier studies, the most unexpected finding of this study pertaining to the ER is the limited amount of interaction between ER cisternae and cell plate membranes that we have been able to detect during the early stages of cell plate formation (i.e., phragmoplast initials and the solid phragmoplast stages of cell plate assembly) (Figures 1B, 1C, 10A, and 10B). It can be argued that because the ER membranes are sometimes difficult to see in high-pressure frozen/freeze-substituted plant cells, we have not been able to detect all of the cell plate–associated membranes in our samples. However, as Figures 10C and 10D (and data not shown) document, we were able to identify large amounts of ER membranes in our tomograms of maturing cell plates (TN to PFS stages) processed identically to those of earlier stages. This gives us confidence that the reduced amount of ER seen in the earlier stage samples is real. We now believe that the discrepancy between our results and those of earlier studies (Hepler and Newcomb, 1967; Hepler, 1982; Brown and Lemmon, 1991, 1992; Schopfer and Hepler, 1991) relates to the difficulty of precisely staging cell plate images in thin sections of chemically fixed specimens owing to the swelling of the callose-containing membrane compartments.

The limited amount of cell plate–associated ER in the stages in which maximum cell plate growth takes place does not support the idea that the ER assists in cell plate growth by providing a cage that holds the vesicles in place for them to fuse (Hepler,

1982). The dispersed strands of ER that do cross the solid phragmoplast cell plate (Figures 10A and 10B) could conceivably help regulate Ca^{2+} levels within the CPAM. Because the amount of cell plate–associated ER increases over time, the most extensive associations of ER and cell plate membranes are seen over the PFSs, for example, after the CPAM breaks down (Figures 10C and 10D). In these regions, the ER is seen to form a TN that parallels the cell plate and connects to the rest of the ER through tubules that extend into the cytoplasm. The thin tubular strands that pass through the cell plate fenestrae are most likely the precursors of plasmodesmata, and the number of such strands increases between the TVN and the fenestrated sheet stages of cell plate development. In some places, patches of ER membrane are seen to become attached to the cell plate membrane via discrete linkers (Figure 10E). In other systems, such contact sites between ER and plasma membrane have been shown to mediate lipid trafficking via a molecular lipid hopping mechanism (Staehelin, 1997).

METHODS

Plant Material

Seeds of Arabidopsis (Landsberg *erecta* wild type) were planted in 0.8% (w/v) agar plates with MS medium (Sigma, St. Louis, MO) for 2 d and then acclimated over a period of 3 d with increasing sucrose concentrations as follows: 50 mM sucrose for 48 h and 100 mM sucrose for 24 h before cryofixation. Seedlings were grown at a temperature of 24°C and a 16-h photoperiod.

High-Pressure Freezing and Freeze Substitution

Shoot and root apical meristems and leaf primordia were excised from 5-d-old seedlings, transferred to aluminum sample holders, cryoprotected with 150 mM sucrose, frozen in a Baltec HPM 010 high-pressure freezer (Technotrade, Manchester, NH), and then transferred to liquid nitrogen. The samples were then freeze substituted in 4% OsO_4 in anhydrous acetone at −80°C for 5 d, followed by slow warming to room temperature over a period of 2 d. After rinsing in several acetone washes, they were removed from the holders, incubated in propylene oxide for 30 min, rinsed again in acetone, and infiltrated with increasing concentrations of Epon resin (Ted Pella, Redding, CA) in acetone according to the following schedule: 4 h in 5% resin, 4 h in 10% resin, 12 h in 25% resin, and 24 h in 50, 75, and 100% resin, respectively. Polymerization was performed at 60°C for 2 d under vacuum.

For protein immunogold labeling, the high-pressure frozen samples were substituted in 0.2% uranyl acetate + 0.25% glutaraldehyde in acetone at −80°C for 10 d and warmed to −60°C for 18 h. After several acetone rinses, samples were removed from the holders and slowly infiltrated at −60°C with Lowicryl HM20 (Electron Microscopy Sciences, Fort Washington, PA) as follows: 1 d each in 10, 25, and 75% HM20 in acetone, respectively. During 3 more days, 100% HM20 was used and was replaced with freshly made resin every 8 h. Finally, samples were polymerized at −50°C under UV light for 72 h. Freeze substitution, Lowicryl embedding, and resin polymerization were performed under controlled time and temperature conditions in a Leica AFS system (Vienna, Austria).

Sample Preparation for Thin-Section Electron Microscopy

Epon thin sections (80 nm thick) were mounted on formvar-coated copper slot grids and stained with 3% uranyl acetate in 70% methanol (10 min) and Reynold's lead citrate (4 min). Approximately 400 EM micrographs of cell plates at different stages were taken and analyzed in parallel with the tomograms.

Immunolabeling of ADL1A

The antibody anti-ADL1A (Kang et al., 2001, 2003; Otegui et al., 2001) was used to detect dynamin-like proteins over the cell plate. Samples embedded in Lowicryl HM20 were sectioned into ∼80-nm-thick sections and placed on formvar-coated nickel slot grids. Immunocytochemistry was performed essentially as described by Seguí-Simarro et al. (2003). Briefly, sections were blocked for 5 min with 5% BSA in PBST (phosphate-buffered saline + 0.1% Tween 20). Anti-ADL1A was diluted 1:20 in 1% BSA in PBST, and sections were incubated for 1 h at room temperature. After several rinses in 1% BSA in PBST, sections were incubated with the secondary antibody (anti-rabbit IgG conjugated to 10-nm gold particles, diluted 1:25 in 1% BSA in PBST) for 1 h. Finally, sections were rinsed three times in PBST and distilled water and counterstained with 3% uranyl acetate in 70% methanol (10 min) and Reynold's lead citrate (2 min). Control experiments were performed by excluding the primary antibody.

Immunolabeling of Callose

We used a monoclonal antibody crossreacting with β-1,3-glucan from Biosupplies (Parkville, Victoria, Australia). Epon-embedded samples were sectioned (80 nm thick), and sections were placed on formvar-coated nickel grids. Immunocytochemical assays were performed essentially as described above, with anti-callose antibody diluted 1:10 in PBST. The secondary antibody used was anti-mouse IgG conjugated to 15-nm gold particles. Controls were performed by excluding the primary antibody.

Sample Preparation for Electron Tomography

Three hundred–nm-thick Epon sections were mounted on formvar-coated copper slot grids and stained as described for thin sections. After the staining, 10-nm colloidal gold particles were added to both sides of the grid to be used as fiducial markers to align the series of tilted images. Both sides of the grids were coated with carbon to enhance stability.

Intermediate/High-Voltage Electron Microscopy and Acquisition of Tilt Series Images

For small tomograms, covering just a single frame, an FEI Tecnai TF30 intermediate voltage EM (FEI, Hillsboro, OR) was used, operating at 300 kV. The images were taken at ×20,000 from +60° to −60° at 1° intervals about two orthogonal axes (Mastronarde, 1997), being collected with a Gatan Megascan 795 digital camera (Gatan, Pleasanton, CA) that covered an area of 2.6 × 2.6 μm² and had a resolution of 2048 × 2048 pixels at a pixel size of 1.26 nm. For larger tomograms, a JEM-1000 high-voltage EM (JEOL, Tokyo, Japan) was used, operating at 750 kV. The software controlling the camera and microscope collected a montage of overlapping frames (3 to 16, depending on the tomogram) at each tilt, repositioning the image and focusing the specimen after each tilt. The images were taken at ×12,000 from +60° to −60° at 1.5° intervals about two orthogonal axes and collected with a Gatan digital camera that covered an area of 1.4 × 1.4 μm² and had a resolution of 1024 × 1024 pixels at a pixel size of 1.42 nm.

A total of 15 tomograms were reconstructed, representing all of the four stages described in this paper. At least three tomograms were obtained for each stage, and at least two tomograms for each stage were calculated from montaged frame images that covered at least a

4.5 × 4.5-μm cell plate area (half of a typical ~10-μm wide Arabidopsis meristem cell plate) and were at least 2 serial sections thick (≥600 nm). Together, all of these tomograms yielded an approximate total of 6700 2-nm-thick tomographic slices. All of these were individually analyzed.

3-D Tomographic Reconstruction and Modeling

The images (single or montaged frames) were aligned using the gold particles as fiducial markers as described by Ladinsky et al. (1999). Each set of aligned tilts was reconstructed into a single-axis tomogram using the R-weighted back-projection algorithm (Gilbert, 1972). Merging the two single-axis tomograms into a dual-axis tomogram involved a warping procedure rather than a single linear transformation (Mastronarde, 1997). This procedure was followed for each of the analyzed sections. For each stage in cell plate development, at least two, sometimes three, of the analyzed sections corresponded to serial sections. These were aligned with each other and combined as described by Ladinsky et al. (1999).

Tomograms were displayed and analyzed with 3dmod, the graphics component of the IMOD software package (Kremer et al., 1996) using PC computers running the Linux Red Hat operating system. Membranous structures, MTs, and all types of vesicles were modeled as described by Ladinsky et al. (1999), Marsh et al. (2001), and Otegui et al. (2001). Once a model was completed, meshes of triangles were computed to define the surface of each object (Kremer et al., 1996).

The initial exposure to the electron beam causes a collapse in the section. Thus, to obtain accurate shapes and numerical data, we applied a correction factor to the Z-scale to stretch the resulting models to the thickness of the original sections analyzed, 300 nm. This correction factor was calculated by dividing the section thickness by the calculated tomographic volume (number of tomographic slices multiplied by the pixel size) and was independently applied only to the Z-scale.

The image slicer tool of 3dmod was used to display and analyze tomographic slices extracted from the tomogram in any position or tilt around the x, y, or z axis. This tool was particularly useful for studying the morphology of the connecting and nonconnecting structures seen in vesicles and the dynamin-like rings and spirals. Additionally, the slicer tool allowed us to obtain squeezed images where a number of consecutive tomographic slices were combined, thus generating Z-projections of different thicknesses, similar to conventional EM thin sections. Individual contours also were combined with the squeezed slices using the slicer tool.

3-D Analysis

All of the volumes and surface areas were calculated using the object meshes and the Imodinfo program. For all of the calculations, it was assumed that the cell plate is a form of plasma membrane and, as Wolfe and Steponkus (1983) hypothesized, that it cannot be expanded by stretching. Vesicles, hourglasses, and dumbbells were modeled independently to obtain their individual values. For all of the stages during cell plate development, we calculated the unit cell plate surface area and volume by extracting randomly located boxes of $1 \times 1 \times 0.3$ μm³ along the cell plate for all of the tomograms corresponding to the same cell plate developmental stage. We calculated the membrane surface area and volume of only those boxes that included the whole thickness of the cell plate. A minimum of 10 boxes were analyzed for each cell plate developmental stage. Multiplying these values by a factor of 3.33, we obtained the unit cell plate surface area and the volume of the cell plate pieces contained in a 1-μm³ box, which were then averaged per stage. The changes in unit cell plate surface area and volume observed between stages also were expressed in terms of vesicle equivalents to estimate the net gain of fusing vesicles or loss of clathrin-coated vesicles needed to progress from one stage to the next. For this, the surface area and volume of dense and light vesicles were calculated from the average measured

diameter of each class, assuming a spherical shape for vesicles. Then, for fusing vesicles, the relative percentage of each type (dense and light) was calculated, and the net gain (after subtracting the values corresponding to the previous stage) in unit cell plate surface area and volume was estimated according to the following formula: net gain = percentage of dense vesicles × number of dense equivalents + percentage of light vesicles × number of light equivalents.

The CPAM width at each stage was calculated by measuring and averaging the distances from 150 ribosomes to the cell plate in all of the tomograms corresponding to the same cell plate developmental stage. Only the ribosomes closest to the cell plate, with no more ribosomes between them and the cell plate, were considered. They were randomly taken at different places around the cell plates.

Availability of Software and Tomogram Files

The IMOD software package can be downloaded from http://bio3D.colorado.edu/imod/.

REFERENCES

Asada, T., Sonobe, S., and Shibaoka, H. (1991). Microtubule translocation in the cytokinetic apparatus of cultured tobacco cells. Nature **350,** 238–241.

Assaad, F.F. (2001). Plant cytokinesis. Exploring the links. Plant Physiol. **126,** 509–516.

Bajer, A.S. (1968). Fine structure studies on phragmoplast and cell plate formation. Chromosoma **24,** 383–417.

Baskin, T.I., and Cande, W.Z. (1990). The structure and function of the mitotic spindle in flowering plants. Annu. Rev. Plant Physiol. Plant Mol. Biol. **41,** 277–315.

Becker, W.A. (1932). Recherches expérimentales sur la cytocinèse et la formation de la plaque cellulaire dans la cellule vivante. C. R. Acad. Sci. Paris **194,** 1850–1852.

Bednarek, S.Y., and Falbel, T.G. (2002). Membrane trafficking during plant cytokinesis. Traffic **3,** 621–629.

Brown, R.C., and Lemmon, B.E. (1991). Pollen development in orchids. 5. A generative cell domain involved in spatial control of the hemispherical cell plate. J. Cell Sci. **100,** 559–565.

Brown, R.C., and Lemmon, B.E. (1992). Pollen development in orchids. 4. Cytoskeleton and ultrastructure of the unequal pollen mitosis in *Phalenopsis.* Protoplasma **167,** 183–192.

Buvat, R., and Puissant, A. (1958). Observations sur la cytodierese et l'origine des plasmodesmes. C. R. Acad. Sci. Paris **247,** 233–236.

Carvalho, P., Tirnauer, J.S., and Pellman, D. (2003). Surfing on microtubule ends. Trends Cell Biol. **13,** 229–237.

Cutler, S.R., and Ehrhardt, D.W. (2002). Polarized cytokinesis in vacuolate cells of Arabidopsis. Proc. Natl. Acad. Sci. USA **99,** 2812–2817.

Cvrckova, F., Elias, M., Hala, M., Obermeyer, G., and Zarsky, V. (2001). Small GTPases and conserved signalling pathways in plant cell morphogenesis: From exocytosis to the exocyst. In Cell Biology of Plant and Fungal Tip Growth, A. Geitmann, M. Cresti, and I.B. Heath, eds (Amsterdam, The Netherlands: IOS Press), pp. 105–122.

Errera, L. (1888). Ueber Zellformen und Seifenblasen. Beihefte z. Botan. Zentralblatt. **34,** 395–398.

Finger, F.P., Hughes, T.E., and Novick, P. (1998). Sec3p is a spatial landmark for polarized secretion in budding yeast. Cell **92,** 559–571.

Fu, D., Libson, A., Miercke, L.J.W., Weitzman, C., Nollert, P., Krucinski, J., and Stroud, R.M. (2000). Structure of a glycerol-conducting channel and the basis for its selectivity. Science **290,** 481–486.

Gilbert, P.F.C. (1972). Reconstruction of a 3-dimensional structure from projections and its application to electron-microscopy II. Direct Methods. Proc. R. Soc. Lond. B Biol. Sci. **182,** 89–102.

Gilkey, J.C., and Staehelin, L.A. (1986). Advances in ultra-rapid freezing for the preservation of cellular ultrastructure. J. Electron Microsc. Tech. **3,** 177–210.

Goldberg, R., Morvan, C., Jauneau, A., and Jarvis, M. (1996). Methylesterification, de-esterification and gelation of pectins in the primary cell wall. In Progress in Biotechnology: Pectins and Pectinases, J. Visser and A.G.J. Voragen, eds (Amsterdam, The Netherlands: Elsevier Science), pp. 151–172.

Gu, X., and Verma, D.P. (1996). Phragmoplastin, a dynamin-like protein associated with cell plate formation in plants. EMBO J. **15,** 695–704.

Gu, X., and Verma, D.P. (1997). Dynamics of phragmoplastin in living cells during cell plate formation and uncoupling of cell elongation from the plane of cell division. Plant Cell **9,** 157–169.

Guertin, D.A., Trautmann, S., and McCollum, D. (2002). Cytokinesis in eukaryotes. Microbiol. Mol. Biol. Rev. **66,** 155–178.

Gunning, B.E.S. (1982). The cytokinetic apparatus: Its developmental and spatial regulation. In The Cytoskeleton in Plant Growth and Development, C. Lloyd, ed (London: Academic Press), pp. 229–292.

Guo, W., Tamanoi, F., and Novick, P. (2001). Spatial regulation of the exocyst complex by Rho1 GTPase. Nat. Cell Biol. **3,** 353–360.

Hepler, P.K. (1982). Endoplasmic-Reticulum in the Formation of the Cell Plate and Plasmodesmata. Protoplasma **111,** 121–133.

Hepler, P.K. (1994). The role of calcium in cell division. Cell Calcium **16,** 322–330.

Hepler, P.K., and Jackson, W.T. (1968). Microtubules and early stages of cell-plate formation in the endosperm of Haemanthus katherinae Baker. J. Cell Biol. **38,** 437–446.

Hepler, P.K., and Newcomb, E.H. (1967). Fine structure of cell plate formation in the apical meristem of Phaseolus roots. J. Ultrastruct. Res. **19,** 499–513.

Hepler, P.K., Palevitz, B.A., Lancelle, S.A., McCauley, M.M., and Lichtscheidl, I. (1990). Cortical endoplasmic reticulum in plants. J. Cell Sci. **96,** 355–373.

Hepler, P.K., Valster, A., Molchan, T., and Vos, J.W. (2002). Roles for kinesin and myosin during cytokinesis. Philos. Trans. R. Soc. Lond., B, Biol. Sci. **357,** 761–766.

Hsu, S.C., Hazuka, C.D., Foletti, D.L., and Scheller, R.H. (1999). Targeting vesicles to specific sites on the plasma membrane: The role of the sec6/8 complex. Trends Cell Biol. **9,** 150–153.

Hsu, S.C., Hazuka, C.D., Roth, R., Foletti, D.L., Heuser, J., and Scheller, R.H. (1998). Subunit composition, protein interactions, and structures of the mammalian brain sec6/8 complex and septin filaments. Neuron **20,** 1111–1122.

Kakimoto, T., and Shibaoka, H. (1992). Synthesis of polysaccharides in phragmoplasts isolated from tobacco BY-2 cells. Plant Cell Physiol. **33,** 353–361.

Kang, B.-H., Busse, J.S., and Bednarek, S.Y. (2003). Members of the Arabidopsis dynamin-like gene family, ADL1, are essential for plant cytokinesis and polarized cell growth. Plant Cell **15,** 899–913.

Kang, B.-H., Busse, J.S., Dickey, C., Rancour, D.M., and Bednarek, S.Y. (2001). The Arabidopsis cell plate-associated dynamin-like protein, ADL1Ap, is required for multiple stages of plant growth and development. Plant Physiol. **126,** 47–68.

Kremer, J.R., Mastronarde, D.N., and McIntosh, J.R. (1996). Computer visualization of three-dimensional image data using IMOD. J. Struct. Biol. **116,** 71–76.

Ladinsky, M.S., Mastronarde, D.N., McIntosh, J.R., Howell, K.E., and Staehelin, L.A. (1999). Golgi structure in three dimensions: Functional insights from the normal rat kidney cell. J. Cell Biol. **144,** 1135–1149.

Lauber, M.H., Waizenegger, I., Steinmann, T., Schwarz, H., Mayer, U., Hwang, I., Lukowitz, W., and Jurgens, G. (1997). The Arabidopsis KNOLLE protein is a cytokinesis-specific syntaxin. J. Cell Biol. **139,** 1485–1493.

Ledbetter, M.C., and Porter, K.R. (1963). A "microtubule" in plant cell fine structure. J. Cell Biol. **19,** 239–250.

Lipschutz, J.H., and Mostov, K.E. (2002). Exocytosis: The many masters of the exocyst. Curr. Biol. **12,** R212–R214.

Liu, B., Lee, Y.R.J., and Pan, R. (2003). Identification of kinesin-related proteins in the phragmoplast. Cell Biol. Int. **27,** 227–228.

Marks, B., Stowell, M.H.B., Vallis, Y., Mills, I.G., Gibson, A., Hopkins, C.R., and McMahon, H.T. (2001). GTPase activity of dynamin and resulting conformation change are essential for endocytosis. Nature **410,** 231–235.

Marsh, B.J., Mastronarde, D.N., Buttle, K.F., Howell, K.E., and McIntosh, J.R. (2001). Organellar relationships in the Golgi region of the pancreatic beta cell line, HIT-T15, visualized by high resolution electron tomography. Proc. Natl. Acad. Sci. USA **98,** 2399–2406.

Mastronarde, D.N. (1997). Dual-axis tomography: An approach with alignment methods that preserve resolution. J. Struct. Biol. **120,** 343–352.

Matern, H.T., Yeaman, C., Nelson, W.J., and Scheller, R.H. (2001). The Sec6/8 complex in mammalian cells: Characterization of mammalian Sec3, subunit interactions, and expression of subunits in polarized cells. Proc. Natl. Acad. Sci. USA **98,** 9648–9653.

Molchan, T.M., Valster, A.H., and Hepler, P.K. (2002). Actomyosin promotes cell plate alignment and late lateral expansion in Tradescantia stamen hair cells. Planta **214,** 683–693.

Mollenhauer, H.H., and Mollenhauer, B.A. (1976). Changes in Golgi apparatus secretory pattern with relation to cell-division in maize root-tips. Plant Physiol. **57,** 10.

Nacry, P., Mayer, U., and Jürgens, G. (2000). Genetic dissection of cytokinesis. Plant Mol. Biol. **43,** 719–733.

Otegui, M.S., Mastronarde, D.N., Kang, B.H., Bednarek, S.Y., and Staehelin, L.A. (2001). Three-dimensional analysis of syncytial-type cell plates during endosperm cellularization visualized by high resolution electron tomography. Plant Cell. **13,** 2033–2051.

Otegui, M.S., and Staehelin, L.A. (2004). 3D Tomographic analysis of post-meiotic cytokinesis during pollen development in *Arabidopsis thaliana.* Planta **218,** 501–515.

Porter, K.R., and Caulfield, J.B. (1958). The formation of the cell plate during cytokinesis in *Allium cepa* L. In Proceedings of the Fourth Congress on Electron Microcopy, Vol. 2. (Berlin, Germany), pp. 503–507.

Porter, K.R., and Machado, R.D. (1960). Studies on the endoplasmic reticulum IV. Its form and distribution during mitosis in cells of onion root tip. J. Biophys. Biochem. Cytol. **7,** 167–180.

Rees, D.A. (1977). Polysaccharide Shapes. (New York: John Wiley & Sons).

Rensing, K.H., Samuels, A.L., and Savidge, R.A. (2002). Ultrastructure of vascular cambial cell cytokinesis in pine seedlings preserved by cryofixation and substitution. Protoplasma **220,** 39–49.

Samuels, A.L., Giddings, T.H., Jr., and Staehelin, L.A. (1995). Cytokinesis in tobacco BY-2 and root tip cells: A new model of cell plate formation in higher plants. J. Cell Biol. **130,** 1345–1357.

Sanderfoot, A.A., Assaad, F.F., and Raikhel, N.V. (2000). The Arabidopsis genome. An abundance of soluble N-ethylmaleimide-sensitive factor adaptor protein receptors. Plant Physiol. **124,** 1558–1569.

Schopfer, C.R., and Hepler, P.K. (1991). Distribution of membranes and the cytoskeleton during cell plate formation in pollen mother cells of *Tradescantia.* J. Cell Sci. **100,** 717–728.

Seguí-Simarro, J.M., Testillano, P.S., and Risueño, M.C. (2003). Hsp70 and Hsp90 change their expression and subcellular localization after microspore embryogenesis induction in *Brassica napus* cv. Topas. J. Struct. Biol. **142,** 379–391.

Sollner, R., Glasser, G., Wanner, G., Somerville, C.R., Jürgens, G., and Assaad, F.F. (2002). Cytokinesis-defective mutants of Arabidopsis. Plant Physiol. **129,** 678–690.

Staehelin, L.A. (1997). The plant ER: A dynamic organelle composed of a large number of discrete functional domains. Plant J. **11,** 1151–1165.

Staehelin, L.A., and Moore, I. (1995). The plant Golgi apparatus—Structure, functional organization and trafficking mechanisms. Annu. Rev. Plant Physiol. Plant Mol. Biol. **46,** 261–288.

Stowell, M.H.B., Marks, B., Wigge, P., and McMahon, H.T. (1999). Nucleotide-dependent conformational changes in dynamin: Evidence for a mechanochemical molecular spring. Nat. Cell Biol. **1,** 27–32.

Strasburger, E. (1875). Über Zellbildung und Zellteilung. (Jena, Germany: Fischer).

TerBush, D.R., Guo, W., Dunkelbarger, S., and Novick, P. (2001). Purification and characterization of yeast exocyst complex. Methods Enzymol. **329,** 100–110.

TerBush, D.R., Maurice, T., Roth, D., and Novick, P. (1996). The Exocyst is a multiprotein complex required for exocytosis in Saccharomyces cerevisiae. EMBO J. **15,** 6483–6494.

Thakur, B.R., Singh, R.K., and Handa, A.K. (1997). Chemistry and uses of pectin—A review. Crit. Rev. Food Sci. Nutr. **37,** 47–73.

Ueda, K., Sakaguchi, S., Kumagai, F., Hasezawa, S., Quader, H., and Kristen, U. (2003). Development and disintegration of phragmoplasts in living cultured cells of a GFP::TUA6 transgenic *Arabidopsis thaliana* plant. Protoplasma **220,** 111–118.

Valster, A.H., Pierson, E.S., Valenta, R., Hepler, P.K., and Emons, A.M.C. (1997). Probing the plant actin cytoskeleton during cytokinesis and interphase by profilin microinjection. Plant Cell **9,** 1815–1824.

van der Bliek,, A.M. (1999). Functional diversity in the dynamin family. Trends Cell Biol. **9,** 96–102.

Verma, D.P., and Hong, Z. (2001). Plant callose synthase complexes. Plant Mol. Biol. **47,** 693–701.

Verma, D.P.S. (2001). Cytokinesis and building of the cell plate in plants. Annu. Rev. Plant Physiol. Plant Mol. Biol. **52,** 751–784.

Waizenegger, I., Lukowitz, W., Assaad, F., Schwarz, H., Jurgens, G., and Mayer, U. (2000). The Arabidopsis KNOLLE and KEULE genes interact to promote vesicle fusion during cytokinesis. Curr. Biol. **10,** 1371–1374.

Whaley, W.G., and Mollenhauer, H.H. (1963). The Golgi apparatus and cell plate formation. A postulate. J. Cell Biol. **17,** 216–221.

Wolfe, J., and Steponkus, P.L. (1983). Mechanical properties of the plasma membrane of isolated plant protoplasts—Mechanism of hyperosmotic and extracellular freezing-injury. Plant Physiol. **71,** 276–285.

Zhang, D., Wadsworth, P., and Hepler, P.K. (1990). Microtubule dynamics in living dividing plant cells: Confocal imaging of micro-injected fluorescent brain tubulin. Proc. Natl. Acad. Sci. USA **87,** 8820–8824.

Zhang, G.F., and Staehelin, L.A. (1992). Functional compartmentation of the Golgi apparatus of plant cells—Immunocytochemical analysis of high pressure frozen and freeze-substituted sycamore maple suspension culture cells. Plant Physiol. **99,** 1070–1083.